Journal of Fluids and Structures (2001) **15,** 171–206
doi:10.1006/jfls.2000.0325, available online at http://www.idealibrary.com on IDEAL®

NONLINEAR FLUID FORCES IN CYLINDRICAL SQUEEZE FILMS. PART II: FINITE LENGTH

Y. HAN

AECL, Chalk River, Ontario, Canada K0J 1JO

AND

R. J. ROGERS

Department of Mechanical Engineering, University of New Brunswick Fredericton, NB, Canada E3B 5A3

(Received 13 June 1999, and in final form 27 June 2000)

Two nonlinear models of finite-length cylindrical squeeze films are developed. The first finite-length model is formed using length-correction factors on a short cylindrical model, while the second finite-length model is constructed using side-leakage factors with an infinitely long model. Each model has seven force terms which are nonlinear functions of instantaneous cylinder position. The two models are evaluated through experimental measurements using two geometrical configurations where 50·6 mm and 25 mm diameter cylinders undergo 160 cases of radial and offset-linear motions. Comparing the theoretical predictions of squeeze force waveforms with measurements, and also with previous models by Lu & Rogers, shows that the present finite-length models are quite reasonable. By investigating each force term, the present models are modified slightly and better predictions are obtained for most test cases. Without empirical corrections, the models tend to underestimate the unsteady inertia terms and are unable to predict the frequency dependence of the viscous terms.
© 2001 Academic Press

1. INTRODUCTION

THERE ARE MANY MECHANICAL COMPONENTS such as shafts or tubes which are loosely supported. Frequently, the annular gaps between such components and their supports are fluid-filled. For journal bearings or squeeze-film dampers, the radial clearance is typically only 0·1% of the radius. For other components such as pipes or tubes, the radial clearance can be much greater, say 2 or 3% of the radius. Vibration of the components due to rotating unbalance or flow-induced vibration results in squeeze-film forces in the annual gaps. In shell-and-tube heat exchangers with liquid shell-side fluids and circular supports, the squeeze-film forces are the main source of damping. Accurate modelling of the squeeze-film forces is very important to be able to predict the dynamic response of the component and wear rates at the supports when metal-to-metal contact occurs.

If the length of the support is short compared to the diameter, the fluid in the clearance space can be assumed to flow in the axial direction. On the other hand, if the support length is long compared to the diameter, the flow is mainly circumferential; the same effect occurs if there are end seals. In either of these extreme cases, closed-form two-dimensional (2-D) solutions of the fluid velocities, pressure and forces can be obtained.

0889–9746/01/010171 + 36 $35.00/0 © 2001 Academic Press

There are many publications about short and long cylindrical squeeze films, which are of great help in understanding the effects of fluid inertia and the mechanics of squeeze flow. The majority of bearings in service and the configuration of tubes and support plates in heat exchangers, however, have length/diameter ratios in the range $0{\cdot}5 < L/D < 1{\cdot}5$; neither the short nor the long cylindrical models can be applied accurately to these designs. The study of finite-length cylindrical models is therefore important for squeeze films used in applications such as rotating machinery and shell-and-tube heat exchangers.

The analytical methods available in the literature for finite-length squeeze films may be classified in three categories, as Capone *et al.* (1994) have stated: (i) methods using length-correction factors with a short bearing solution, for example, Barrett *et al.* (1980); (ii) methods using side-leakage factors with an infinitely long bearing solution, where the widely accepted method is from Warner (1963) [Tichy (1987), San Andres & Vance (1987*a*), Lu (1993), and Zhang & Roberts (1996) have used the same or similar ideas to account for the length effects]; and (iii) methods using a variational approach with a Fourier series expansion, where Hays (1959) may be a good example. Most of the publications in these three categories deal with small to moderate squeeze-film Reynolds number flow. Therefore, fluid inertia is usually neglected to simplify the analysis or else only temporal inertia is considered. The accuracy of these methods has been verified for squeeze films with small Reynolds numbers either through analysis or experimental tests.

Until now, no existing publications can be found which consider theoretically both the finite-length effects with arbitrary cylinder motions and the different kinds of inertia in squeeze-film damper-like structures. The studies of squeeze-film effects in heat exchangers by Mulcahy (1980), Haslinger *et al.* (1990) and many others have shown the requirements of this kind of study and also revealed that, without the aid of some approximations, even the existing models are impossible to solve for some specific motions. Lu & Rogers (1994) used side-leakage factors to obtain finite-length squeeze-film forces from an infinitely long model for radial motions. The comparison between their theoretical results and experimental measurements showed that the length-correction method is quite practical.

There have been numerous experimental investigations performed on squeeze-film dampers used in rotating machinery, which are useful references for other squeeze-film applications such as shell-and-tube heat exchangers. Examples can be seen in publications by Tonnesen (1976), Tichy (1985), San Andres & Vance (1987c), Kinsale & Tichy (1989), Rouch (1990), Arauz & San Andres (1993), and Zhang *et al.* (1994).

By comparison, there are few publications of experimental squeeze-film studies for heat exchanger applications. Recent experimental studies of cylindrical squeeze films with water are given by Rogers *et al.* (1990), Haslinger *et al.* (1990), Yu & Rogers (1991) and Lu & Rogers (1994, 1995). In Lu & Rogers (1994), the normal instantaneous squeeze-film force for a finite length cylinder was measured for a cylinder with radial motions with zero or nonzero initial eccentricity. In Lu & Rogers (1995), instantaneous normal and tangential squeeze-film forces for offset quasi-linear motion and elliptical motion were measured for a system with $L/D = 1$.

In order to gain further physical insight about finite-length squeeze films, correction factors for both short and infinitely long models are used in the present study to obtain finite-length squeeze-film force models. The length-correction factor and side-leakage factor methods used here closely follow the papers of Barrett *et al.* (1980) and Warner (1963). To validate the two models, a total 160 experimental tests were carried out. Two diameters of 50·6 and 25 mm were used to study geometrical scaling effects. Radial motions from either a centred or an eccentric position were first investigated. Similar to tests of circular-centred journal motions in squeeze-film dampers [e.g., San Andres & Vance (1987c) or Jung *et al.* (1991)], simple radial motions are very useful for the current experimental squeeze-film

studies, since only some, in this case three of the seven, force terms are involved. Following the radial motion studies, quasi-straight-line motion with initial eccentricity perpendicular to the motion direction (called offset-linear motion) was used to evaluate the remaining force terms. This motion involves all the normal and tangential force terms and is easier to perform than other general motions, since only one shaker is required.

2. FIRST MODEL: USING LENGTH-CORRECTION FACTORS WITH A SHORT MODEL

Figure 1 shows the cylindrical squeeze-film configuration for a finite-length model with length/diameter ratio in the range $0{\cdot}5 < L/D < 1{\cdot}5$ and the coordinates used. The Reynolds equation for a finite-length squeeze film can be expressed (Szeri 1980) as

$$\frac{1}{R^2}\frac{\partial}{\partial\theta}\left(h^3\frac{\partial p}{\partial\theta}\right)+\frac{\partial}{\partial x}\left(h^3\frac{\partial p}{\partial x}\right)=6\mu E, \tag{1}$$

where

$$-L/2 \le x \le L/2, \quad h = c - e\cos\theta,$$

$$E=\frac{1}{R}\frac{\partial}{\partial\theta}(Uh)-2V, \quad U=e\dot{\psi}\cos\theta-\dot{e}\sin\theta, \quad V=\frac{\mathrm{d}h}{\mathrm{d}t}=-e\dot{\psi}\sin\theta-\dot{e}\cos\theta;$$

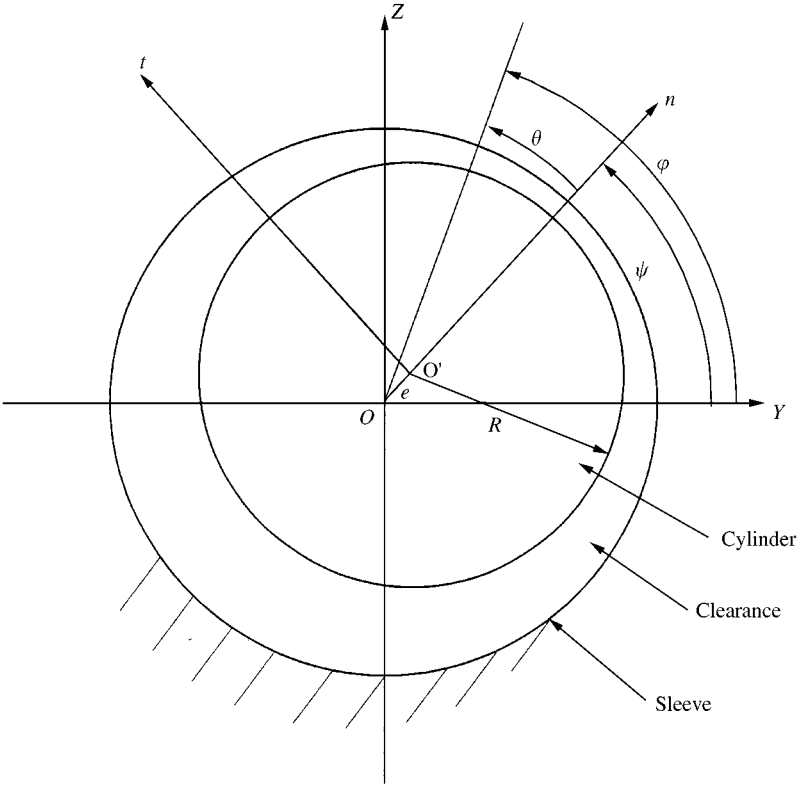

Figure 1. Configuration of finite-length cylindrical squeeze film with arbitrary motion.

see Nomenclature in Appendix B for variable definitions. Following the idea from Barrett *et al.* (1980) and employing variable separation techniques (Massey 1977), the pressure in the squeeze-film flow is obtained as

$$p(\theta, x) = -a\left(\frac{R}{b}\right)^2\left[1 - \frac{\cosh(bx/R)}{\cosh(bL/D)}\right], \tag{2}$$

where

$$a = \frac{6\mu E}{h^3}, \qquad b^2 = -\frac{1}{h^3 p_c}\frac{\partial}{\partial\theta}\left(h^3\frac{\partial p_c}{\partial\theta}\right).$$

The coefficient a is proportional to p_c, the mid-plane ($x = 0$) pressure of the cylindrical squeeze film. The rest of the right-hand side of equation (2) acts as a length correction factor. Equation (2) can be considered as an exact expression of the pressure for the finite-length squeeze film without considering the inertia effects.

When $L/D \ll 1$, equation (2) reduces to the expression for a short model (Barrett *et al.* 1980), so that

$$\left(\frac{R}{b}\right)^2\left[1 - \frac{\cosh(bx/R)}{\cosh(bL/D)}\right] \approx \frac{L^2}{8}\left(1 - \frac{4x^2}{L^2}\right). \tag{3}$$

The mid-plane pressure for the short model derived from Reynolds' equation is given by

$$p_{sc}(\theta) = \frac{3\mu L^2}{2h^3}(e\dot{\psi}\sin\theta + \dot{e}\cos\theta) = -\frac{3\mu L^2}{2h^3}V \approx \frac{3\mu L^2 E}{4h^3} = \frac{aL^2}{8}, \tag{4}$$

where the approximation is achieved by neglecting terms of the order h/R in the expression for E below equation (1). Using expressions (3) and (4) in equation (2), gives $p(\theta, x)$ for the short-length model

$$p(\theta, x) = p_{sc}(\theta)\left(1 - \frac{4x^2}{L^2}\right); \tag{5}$$

this is essentially as in Burwell (1951).

As an alternative, one may keep the expression for $a \approx 8p_{sc}(\theta)/L^2$, together with the original hyperbolic length correction function of x, to obtain the approximate equation from Barrett *et al.* (1980) for the pressure in the finite-length squeeze-film bearing

$$p(\theta, x) = \frac{8p_{sc}(\theta)R^2}{L^2}\left(\frac{1}{b}\right)^2\left[1 - \frac{\cosh(bx/R)}{\cosh(bL/D)}\right]. \tag{6}$$

Because $a \approx 8p_{sc}(\theta)/L^2$ is for a short bearing, not for a finite-length bearing, equation (6) should be more accurate for small bearing lengths close to a short bearing. This is also shown by the numerical study by San Andres & Vance (1987*b*).

To employ equation (6) in the application of arbitrary cylinder motion, a similar form of nondimensional length-correction factors as in the paper by Barrett *et al.* (1980)

$$L^m = \left(\frac{1}{b_m}\right)^2\left[1 - \frac{\cosh(b_m x/R)}{\cosh(b_m L/D)}\right] \qquad (m = n \text{ or } t) \tag{7}$$

has been used here for the normal and tangential directions. (Actually, to call them length factors is more accurate, since $p_c(\theta)$ is only a centreline pressure.) In the above equation, the b_m are calculated using the pressure expressions obtained from the infinitely long model

approximation of Reynolds equation for circular-centred and radial motions. Based on the study by Barrett *et al.* (1980), for circular-centred motion b_t is given by

$$b_t^2 = \frac{(2+\varepsilon^2)}{(1+\varepsilon\cos\theta)(2+\varepsilon\cos\theta)}. \tag{8}$$

Substituting the above expression into equation (6) and integrating the pressure along the cylinder surface fails to yield a closed-form analytical expression for the force. In order to eliminate the dependence on θ, the following averaging is defined in the present study:

$$b_t^2 = \frac{1}{\pi}\int_0^{\pi} \frac{(2+\varepsilon^2)}{(1+\varepsilon\cos\theta)(2+\varepsilon\cos\theta)}\,\mathrm{d}\theta. \tag{9}$$

Integrating this equation yields

$$b_t^2 = (2+\varepsilon^2)\,[(1-\varepsilon^2)^{-1/2} - (4-\varepsilon^2)^{-1/2}]. \tag{10}$$

Note the erratum note regarding this expression in Appendix A. Similarly, referring to the paper by Barrett *et al.* (1980) for radial motion, we can obtain

$$b_n^2 = \frac{2}{\pi\varepsilon^2}\left(\pi + \frac{(\pi-\gamma_1)(2+\varepsilon^2)}{(1-\varepsilon^2)^{1/2}} - \frac{(\pi-\gamma_2)(8+\varepsilon^2)}{(4-\varepsilon^2)^{1/2}}\right), \tag{11}$$

where γ_1 and γ_2 have values between 0 and $\pi/2$ and are expressed as

$$\gamma_1 = \tan^{-1}\frac{\gamma}{\varepsilon} \quad \text{and} \quad \gamma_2 = \tan^{-1}\frac{(4-\varepsilon^2)^{1/2}}{\varepsilon}.$$

Using the pressure equation for the short model derived by Han & Rogers (2001), the pressure for the finite-length model can now be expressed as

$$\begin{aligned} p(\theta,x) - p_a = {} & \left(\frac{D_1\mu\cos\theta}{c^3(1-\varepsilon\cos\theta)^3}\,\dot{e} + \frac{D_2\rho\cos\theta}{c(1-\varepsilon\cos\theta)}\,\ddot{e} + \frac{D_3\rho\cos^2\theta}{c^2(1-\varepsilon\cos\theta)^2}\,\dot{e}^2\right) R^2 L^n \\ & + \left(-\frac{D_2\rho\cos\theta}{c(1-\varepsilon\cos\theta)}\,e\dot{\psi}^2 + \frac{D_1\mu\sin\theta}{c^3(1-\varepsilon\cos\theta)^3}\,e\dot{\psi} + \frac{D_2\rho\sin\theta}{c(1-\varepsilon\cos\theta)}\,e\ddot{\psi}\right. \\ & \left. + \frac{D_3\rho\sin^2\theta}{c^2(1-\varepsilon\cos\theta)^2}\,(e\dot{\psi})^2\right) R^2 L^t \\ & + \left(\frac{D_2\rho\sin\theta}{c(1-\varepsilon\cos\theta)}\,2\dot{e}\dot{\psi} + \frac{D_3\rho\cos\theta\sin\theta}{c^2(1-\varepsilon\cos\theta)^2}\,2e\dot{e}\dot{\psi}\right) R^2\,\frac{(L^n+L^t)}{2}, \end{aligned} \tag{12}$$

where the terms in large brackets are comparable to the a factor in equation (2), the D_i ($i = 1, 2, 3$) coefficients depend on the velocity profile assumed, as well as the approximation method (Han & Rogers 1996), and L^n and L^t are the length-correction factors defined in equation (7) for radial and tangential motions of the cylinder centre, respectively; $(L^n + L^t)/2$ on the last term is used to consider the combined effect of the motions. Other combined weightings such as $(L^n \cdot L^t)^{1/2}$ were considered, however such expressions would make integration to obtain analytical force expressions more difficult.

The elementary radial squeeze-film force on an arc of width $R\,\mathrm{d}\theta$ in the finite-length model is

$$\mathrm{d}F_f = \int_{-L/2}^{L/2} (p(\theta,x) - p_a)\,R\,\mathrm{d}\theta\,\mathrm{d}x. \tag{13}$$

The forces acting on the moving cylinder in the normal n and tangential t directions can be written as

$$F_n = -\int_0^{2\pi} \cos\theta \, \mathrm{d}F_f, \qquad F_t = -\int_0^{2\pi} \sin\theta \, \mathrm{d}F_f. \tag{14, 15}$$

Integrating the above two equations using Booker's (1965) integral table, the force equations for the first finite-length model can be expressed as

$$F_n = -12\left(\frac{R}{L}\right)^2 \left(L_s^n C_1 C_v^n \dot{e} + L_s^n C_2 M_{un}^n \ddot{e} + L_s^n C_2 M_{cv} \frac{\dot{e}^2}{e} - L_s^t C_2 M_{ce} e \dot{\psi}^2 \right), \tag{16}$$

$$F_t = -12\left(\frac{R}{L}\right)^2 \left(L_s^t C_1 C_v^t e\dot{\psi} + L_s^t C_2 M_{un}^t e\ddot{\psi} + (L_s^n + L_s^t) C_2 M_{co} \dot{e}\dot{\psi} \right), \tag{17}$$

where the geometry coefficients $C_1 = \mu L^3 R/c^3$, $C_2 = \rho L^3 R/c$ and the nonlinear force coefficients C_v^n, M_{un}^n, M_{cv}, M_{ce}, C_v^t, M_{un}^t and M_{co} are given in Han & Rogers (2001). Because of the C_1 and C_2 coefficients, the ratio of any inertia term to any viscous term is proportional to c^2. The length-correction factors after integrating equation (13), and considering motions in the radial and tangential directions, are expressed as

$$L_s^m = \frac{1}{(b_m)^2}\left[1 - \frac{\tanh(b_m L/D)}{b_m L/D}\right] \qquad (m = n \text{ or } t). \tag{18}$$

As L/D approaches zero, the factors $12(R/L)^2 L_s^m$ and $12(R/L)^2(L_s^n + L_s^t)/2$ increase towards unity, so that equations (16) and (17) approach the force expressions for short cylindrical squeeze films.

3. SECOND MODEL: USING SIDE-LEAKAGE FACTORS WITH THE INFINITELY LONG MODEL

The more familiar and widely accepted form of obtaining the pressure or force expressions for finite-length bearing dampers is to use side-leakage factors on an infinitely long model solution. The side-leakage factor is given by Warner (1963):

$$L_l^m = 1 - \frac{\tanh(\lambda_l^m L/D)}{\lambda_l^m L/D}, \tag{19}$$

where l can be ce, co, cv, un, or v, and m represents n or t, respectively, for normal or tangential direction. Since it is very similar to the length-correction factor used for the short-length model, this side-leakage factor should be able to take into account different kinds of motions and length effects. Because of the difficulty of obtaining the eigenvalues λ_l^m from the boundary value problem, different specific motion cases have been worked out. Tolle & Muster (1969) determined the eigenvalues for the normal and tangential motions of the journal centre for the pure viscous case. Falkenhagen *et al.* (1972) derived the λ_l^m based on Reynolds' equation for steady-state circular centred motion. No existing results of the eigenvalues can be found considering the inertia effects for general motion of the journal bearing centre. San Andres & Vance (1987*a*, *b*) proposed the following method to determine the eigenvalues for circular centred motion:

$$L_l^m \,(\text{Force term of long model})_{L/D \to 0} = (\text{Force term of short model}). \tag{20}$$

TABLE 1
Eigenvalues for the side-leakage factors obtained using equation (21)*

λ_v^n	$\dfrac{\sqrt{1+2\varepsilon^2}}{\gamma}$	λ_v^t	$\dfrac{\gamma}{\sqrt{3}(1-\varepsilon)}$
λ_{un}^n	$\dfrac{1}{\sqrt{\gamma}}$	λ_{un}^t	$\sqrt{\dfrac{\gamma(1-\gamma)}{(1-2\varepsilon)(1-\gamma)+\varepsilon^2}}$
λ_{cv}	$\sqrt{\dfrac{D_3}{\gamma^3}\dfrac{2-3\varepsilon^2-2\gamma^3}{\beta_{cv}}}$	λ_{co}	$\sqrt{\dfrac{2(1-\gamma)(1+\varepsilon)(D_2\gamma+D_3(1-\gamma))}{\beta_{co}}}$
λ_{ce}	$\sqrt{\dfrac{1-\gamma}{\gamma}\dfrac{D_2-D_3(1-\gamma)}{\beta_{ce}}}$		

*Note: In the table

$$\beta_{cv} = D_3\left(2-\frac{2-\varepsilon^2}{\gamma}\right)+D_4\left(\frac{6-3\varepsilon^2}{2\gamma}-3\right),$$

$$\beta_{ce} = D_2(1-\gamma)-D_3\left(2-\varepsilon-\frac{(1-\varepsilon)(2+\varepsilon)}{\gamma}\right)-D_4\left(2\varepsilon-3+\frac{(1-\varepsilon)(8\varepsilon+\varepsilon^2+6)}{2\gamma(1+\varepsilon)}\right),$$

$$\beta_{co} = D_2(2-\varepsilon-2\varepsilon^2+\varepsilon^3-2\gamma+\varepsilon\gamma+3\varepsilon^2\gamma)+D_3(-4-\varepsilon+5\varepsilon^2+4\gamma+\varepsilon\gamma-3\varepsilon^2\gamma)$$
$$-D_4(-6-2\varepsilon+7\varepsilon^2+6\gamma+2\varepsilon\gamma-4\varepsilon^2\gamma+\varepsilon^3).$$

The side-leakage factor L_l^m can be approximately expressed by writing equation (19) as a partial Taylor series

$$L_l^m = (\lambda_l^m L/D)^2/3. \tag{21}$$

The good accuracy of the method is demonstrated by comparing the analytical solutions with the results from finite-element solutions for most configurations of squeeze-film dampers and different orbit radii considered in a later publication by the same authors (San Andres & Vance 1987*c*).

Based on the same idea, the force expression for the second finite-length model, obtained by applying the side-leakage factor to an infinitely long model (Han & Rogers 2001), can be written as

$$F_n = -C_1C_v^nL_v^n\dot{e} - C_2M_{un}^nL_{un}^n\ddot{e} - C_2M_{cv}L_{cv}\frac{\dot{e}^2}{e} + C_2M_{ce}L_{ce}e\dot{\psi}^2, \tag{22}$$

$$F_t = -C_1C_v^tL_v^te\dot{\psi} - C_2M_{un}^tL_{un}^te\ddot{\psi} - C_2M_{co}L_{co}2\dot{e}\dot{\psi}. \tag{23}$$

Now $C_1 = \mu R^3L/c^3$ and $C_2 = \rho R^3L/c$. Using the above procedure [equations (20) and (21)], the approximate eigenvalue for each side-leakage factor in equations (22) and (23) was determined and is listed in the Table 1. As L/D tends to infinity, all the L_l^m factors increase toward unity so that equations (22) and (23) approach the force expressions for a long cylindrical squeeze film.

4. EXPERIMENTAL EQUIPMENT AND DATA ACQUISITION

The experimental test rig for measuring cylindrical squeeze-film forces was designed and built by Lu & Rogers (1994). The apparatus has been described previously (Lu & Rogers,

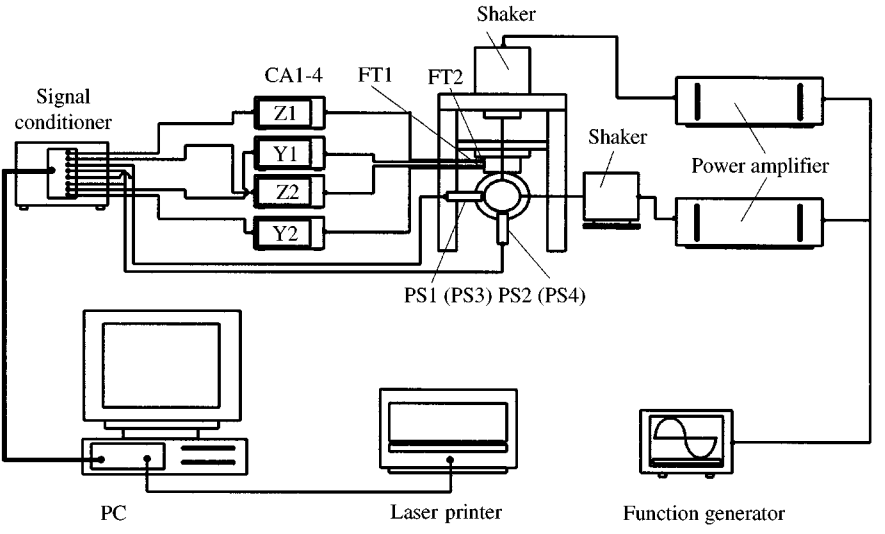

Figure 2. Schematic diagram of data acquisition system set-up. FT: Force Transducer—Kistler 9251A; PS: Proximity Sensor—Bently Nevada 7200; CA: Charge Amplifier—PCB 462A.

1994, 1995). Using this test-rig, Lu (1993) demonstrated the validity of his finite-length cylindrical model for radial motions and his short model for both radial and arbitrary motions. The experimental test rig and the data acquisition instruments have been modified and adjusted to meet new experimental investigation requirements. Figure 2 shows the instrumentation arrangement used for the measurement of the test-rig forces and displacements.

The fluid film forces are measured directly using two triaxial piezoelectric force transducers (Kistler 9251A) which satisfy moment requirements and provide high accuracy for the test-rig alignment, as well as for the measurements. The two Y-direction and two Z-direction picoCoulomb charge signals from the force transducers (FT) pass through four charge amplifiers to be converted into low-impedance voltage signals. The output voltages of the proximity sensors (PS) (Bently Nevada 7200 series) and the signals of the force components go through a signal conditioning box (National Instruments SCXI-1000). The signals then go to a data acquisition (DAQ) board (AT-MIO-16E-2) inserted in a 486 personal computer, where the signals are monitored, manipulated and processed using custom-made LabVIEW software. The A/D converter resolution of the data acquisition board is 12 bits or 4.9 mV. To have accurate absolute fluid viscosity, a thermocouple (Fluke 3830349) was used to measure the temperature of the water in the tank. The temperature was then input into the corresponding LabVIEW program to calculate the absolute fluid viscosity.

To calculate the squeeze-film forces acting on the moving cylinder using the theoretical force equations, the displacement signals $e(t)$ (in both Y and Z directions) are synthesized in the present study by using the Fourier series parameters

$$e(t) = \sum_{i=1}^{n} e_i \cos(2\pi f_i t + \varphi_i) + e_0, \tag{24}$$

where e_i and φ_i are the ith Fourier series parameters of the measured $e(t)$ obtained by using the LabVIEW program. f_i is the ith order frequency, n is the finite order of the Fourier

series, and e_0 is the mean value of the displacement signal. In the present work $n = 8$ was used. The instantaneous velocity and acceleration of the cylinder centre are then obtained by differentiating the above equation. This method avoids the amplification of noise which occurs when raw displacement signals are differentiated.

The two geometrical configurations listed in Table 2 were used. The length/diameter ratios are nearly equal to 1 and the clearance/radius ratio is close to 0·03 in order to represent common tube and support plate proportions in shell-and-tube heat exchangers. The large configuration is both easier to align and has larger force signals. The larger clearance produces larger values of squeeze Reynolds number at low speeds so that significant effects of fluid inertia are easily produced. On the other hand, the size of the small-diameter cylinder is closer to the size of tubes in heat exchangers. Therefore, the experimental results from using the small geometrical configuration may be more useful for the design of heat exchangers.

Table 3 shows the combinations of test frequency, type of motion, initial eccentricity and nondimensional oscillation amplitude for all the experimental test cases. There are 84 test cases for the large geometry and 76 cases for the small geometry. The frequency ranges of 4–32 Hz for the large configuration and 8–64 Hz for the small one were chosen with the aim to have significant squeeze film forces and also to cover the common tube vibration

TABLE 2
Geometrical configurations of the tested squeeze films (mm)

	Large Geometry	Small Geometry
Cylinder diameter	50·60	25·00
Sleeve inside diameter	52·18	25·76
Sleeve length	51·33	25·00
Radial clearance	0·79	0·38

TABLE 3
Experimental test cases for the two configurations

Cylinder diameter (mm)	Frequency (Hz)	Motion type	Initial eccentricity (ε_i)	Amplitude (ε_o)
50·6	4, 8, 16, 32	Radial	0	0·4, 0·6, 0·8
			0·4	0·2, 0·4, 0·5
			0·6	0·2, 0·3
		Offset-linear	0·3	0·4, 0·6, 0·8
			0·4	0·4, 0·6, 0·8
			0·5	0·4, 0·6, 0·7
			0·6	0·4, 0·6
			0·7	0·4, 0·5
25	8, 16, 32, 64	Radial	0	0·4, 0·6, 0·8
			0·4	0·2, 0·4
			0·6	0·2
		Offset-linear	0·3	0·4, 0·6, 0·8
			0·4	0·4, 0·6, 0·8
			0·5	0·4, 0·6, 0·7
			0·6	0·4, 0·6
			0·7	0·4, 0·5

frequency range. The radial motion tests were conducted using the horizontal shaker with the initial eccentricity determined by the position of the micrometer on the translation stage and the proximity sensor readouts. The offset-linear motions were produced by using the vertical shaker with the horizontal eccentricity ratios ranging from $\varepsilon_i = 0{\cdot}3$ to $0{\cdot}7$. Since the effects of any misalignment of the cylinder to the sleeve are more clearly shown by discrepancies between the force measurements and predictions for the offset-linear motion than for radial motion, all four proximity sensors were used; the displacement signals from each end of the cylinder were averaged.

Based on the study by Han (1997), the squeeze-film force equations with an elliptical velocity profile appear to give slightly more accurate results for the squeeze film between a tube and its support plate. Therefore, the comparison of force results is based on the equations with an elliptical velocity profile. The constant coefficients from the iterative method with $A = 1{\cdot}2$ (elliptical profile factor) are used, which are $D_i = 12$, $1{\cdot}180$, $2{\cdot}775$ and $1{\cdot}466$. This case provides the best agreement with measured results. In order to compare the theoretical models with experimental waveforms, Lu & Rogers' (1995) multiple determination coefficient R^2 is used,

$$R^2 = 1 - \frac{\sum_{i=1}^{N} (Y_i - \hat{Y}_i)^2}{\sum_{i=1}^{N} Y_i^2}, \tag{25}$$

where Y_i and $\hat{Y}_i$ are the measured and predicted force values at one instant in time, respectively, and N is the total number of the data points of each waveform.

The following experimental results are divided into two parts. Section 5 gives the results for radial motions and Section 6 presents the offset-linear motion results. Both sections discuss results for both the large geometry (LG) tests and for the small geometry (SG) tests.

5. EXPERIMENTAL RESULTS AND COMPARISONS FOR RADIAL MOTIONS

For convenience, we refer to the finite-length model based on the short model with length-correction factors as the "first finite-length model". The "second finite-length model" refers to the model based on the long model with side-leakage factors. The measured squeeze-film forces are compared with the two theoretical predictions from the present study and also with Lu's modified theoretical models. To improve the prediction accuracy of the present finite-length models, some simple modifications are made based on evaluations of each force term.

For radial motion, the squeeze-film force equations for both finite-length models reduce to

$$F = -D_g\left(C_1 C_v^n L_v \dot{e} + C_2 M_{un}^n L_{un} \ddot{e} + C_2 M_{cv} L_{cv} \frac{\dot{e}^2}{e}\right), \tag{26}$$

where L_v, L_{un} and L_{cv} take the corresponding length-correction or side-leakage factors and D_g is $12(R/L)^2$ for the first model and 1 for the second model.

Lu's modified finite-length model for radial motions can be expressed as (Lu & Rogers 1994)

$$F_n = -\alpha_1 L_1(\beta_1|\varepsilon| + \beta_2 \mathrm{Re}_i)\frac{\mu R^3 L}{c^3}\frac{12\pi}{\gamma^3}\dot{e} - \alpha_2 L_2 \frac{\rho R^3 L}{c}\frac{2\pi(1-\gamma)}{\varepsilon^2}\ddot{e}$$
$$- \alpha_3 L_3 \frac{\rho R^3 L}{c}\frac{8\pi(1-\gamma)^2}{5\varepsilon^2\gamma}\frac{\dot{e}^2}{e}, \tag{27}$$

where $\alpha_1 = 1{\cdot}03$, $\alpha_2 = 1{\cdot}31$, $\alpha_3 = 1{\cdot}59$, $\beta_1 = 0{\cdot}73$, and $\beta_2 = 0{\cdot}23$ are constant correction coefficients obtained for the large geometry configuration. $\mathrm{Re}_i = \rho|\dot{e}|c/\mu$ is the instantaneous Reynolds number and $L_i = 1 - \tanh(\lambda_i L/D)/(\lambda_i L/D)$ $(i = 1, 2, 3)$ are side-leakage factors. The eigenvalues λ_i in the side-leakage expressions can be found in Lu & Rogers (1994).

One point that should be mentioned here is that the force and displacement sensors were recalibrated before the present experimental tests. The sensitivity values of the force and the displacement sensors are about 6% higher and 7% lower, respectively, than the sensitivity values Lu used in his experimental study. These differences in sensitivities result in about 13% underestimation by Lu's theoretical predictions compared to the present experimental measurements.

5.1. Radial Motions with Large Geometry

Figure 3 shows typical large-geometry experimental force results and predicted force waveforms from the three theoretical models for radial motions with zero initial eccentricity and nondimensional oscillation amplitude $\varepsilon_o = 0{\cdot}6$. Figure 4 shows the measured and

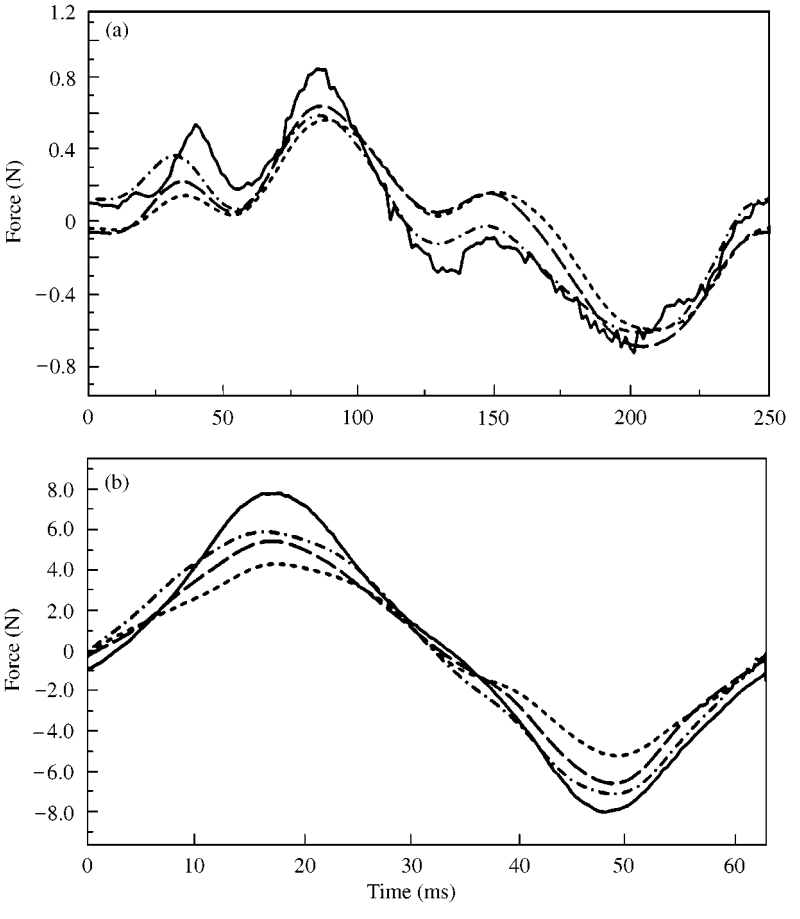

Figure 3. LG squeeze-film forces for radial motion with $\varepsilon_o = 0{\cdot}6$: (a) $f = 4$ Hz; (b) $f = 16$ Hz; ——, Measured; ·–·–·, Lu's model; - - - -, 1st finite; — —, 2nd finite.

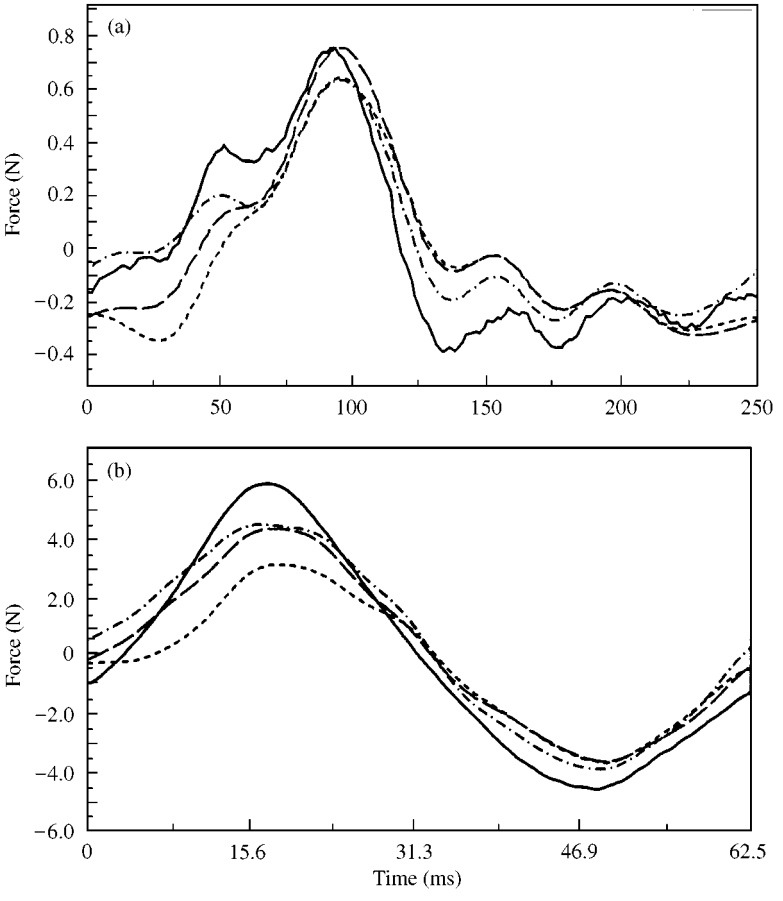

Figure 4. LG forces for radial motion with $\varepsilon_i = 0{\cdot}4$ and $\varepsilon_o = 0{\cdot}4$: (a) $f = 4$ Hz; (b) $f = 16$ Hz; ——, Measured; ·–·–·, Lu's model; - - - -, 1st finite; — —, 2nd finite.

predicted force waveforms for the cylinder vibration with initial eccentricity $\varepsilon_i = 0{\cdot}4$, amplitude $\varepsilon_o = 0{\cdot}4$ and two different frequencies. Figure 5 shows the multiple determination coefficients R^2 for 20 large-geometry cases.

From such graphs, we found: (i) the agreement between the experimental measurements and the theoretical predictions from Lu's model and the present finite-length models are reasonably good; (ii) all the theoretical predictions have similar tendencies for various vibration eccentricities and frequencies; (iii) all the theoretical predictions tend to slightly underestimate the peak force values; (iv) comparing the two present models, the second finite-length model produces better predictions; (v) better agreement between the experimental measurements and theoretical predictions are found for the cases with frequencies $f = 8$ and 16 Hz for all three models; (vi) as the eccentricity values increase, the theoretical under-predictions increase; (vii) there are some slight phase shifts in the cases with vibration frequencies $f = 4$ and 8 Hz; and (viii) for the cases with low frequencies (4 Hz) the experimental squeeze-film forces are small ($< 1{\cdot}0$ N for the case shown in Figure 3) for small eccentricity and some noise can be seen, even though time averaging was performed.

Some exploration to modify the original theoretical equations has been done. Figure 6 shows all the force terms, their resultant forces and the experimental measurements for one

period for the first and second finite-length models for the case $\varepsilon_i = 0{\cdot}4$, $\varepsilon_o = 0{\cdot}4$ and $f = 16$ Hz. The trace of cylinder oscillation in the horizontal direction is also shown.

From the many cases conducted for radial motion with zero initial eccentricity, the underpredicted values were found to be mainly due to the underprediction of the unsteady inertia force term. Since the ratio of acceleration to velocity magnitudes equals the frequency of motion, the dominant effect of the unsteady inertia term is more clear for vibration with higher frequency. The present force equations have been modified slightly by dividing b_n in equation (11) by a constant factor α_{L1} in the first finite-length model and by multiplying the unsteady inertia term in the second model by a constant factor α_{u2}^n. We found that $\alpha_{L1} = 2$ and $\alpha_{u2}^n = 1{\cdot}3$ give much better results.

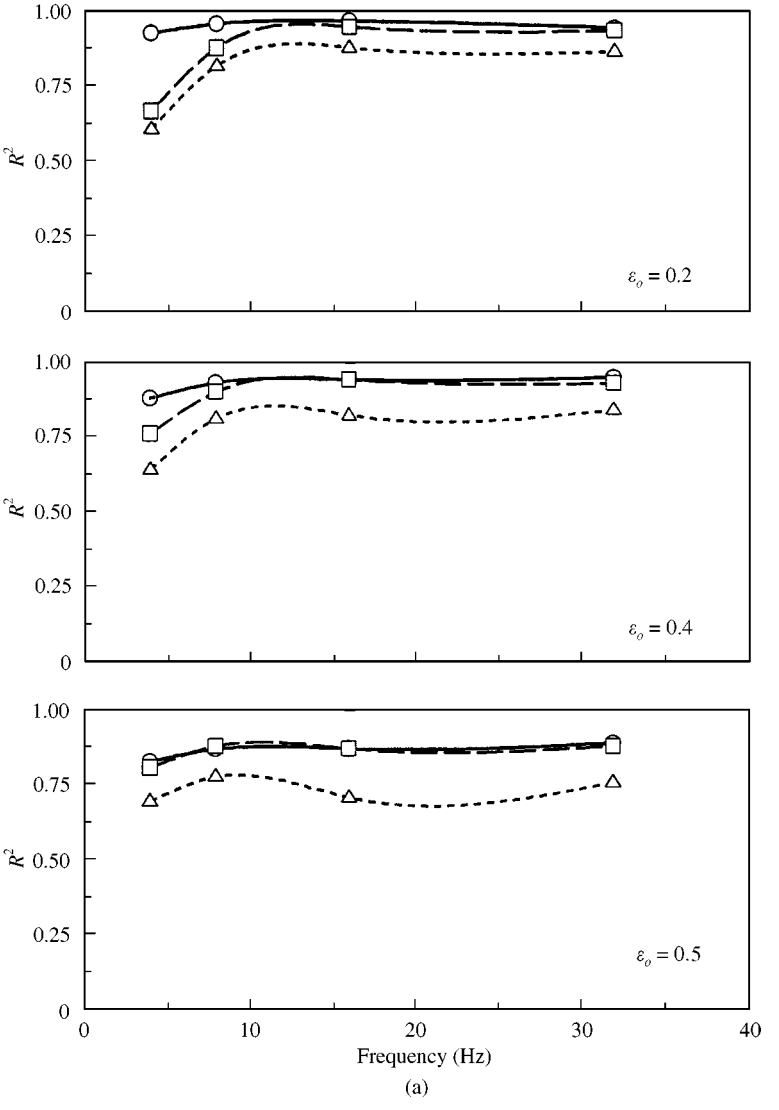

Figure 5. R^2 for LG radial motions with initial eccentricity: (a) $\varepsilon_i = 0{\cdot}4$; (b) $\varepsilon_i = 0{\cdot}6$; —○—, Lu's model; - - -△- - -, first finite; —□—, second finite.

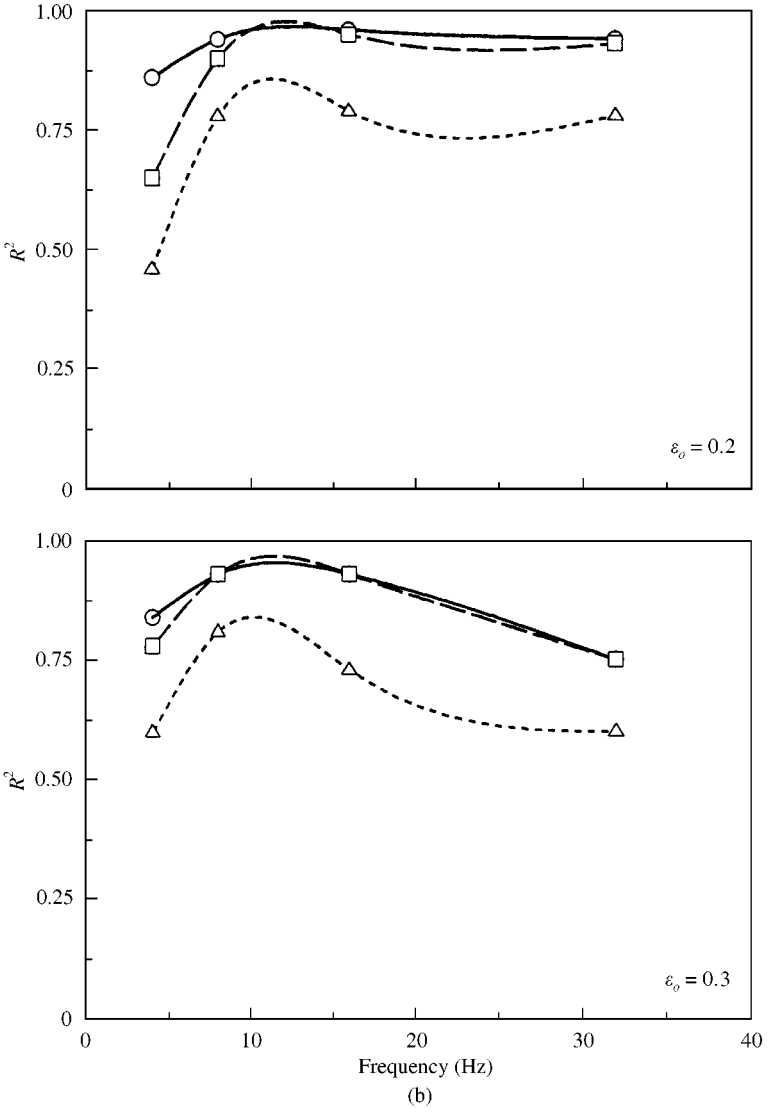

Figure 5. Continued

Even though the contributions to the resultant forces from the viscous terms are small compared with the unsteady inertia terms, through investigating all the test cases, we found the phase shift to be proportional to the viscous terms. The first finite-length model can be improved by multiplying the viscous term by $\alpha_{v1}^n = f/36 + 0{\cdot}2$. [A similar linear function of frequency was used by Lu & Rogers (1994) to correct the viscous term.] No similar modification is applied to the second finite-length model since here the viscous term causes less phase effects and since no simple factor could be found.

Applying these correction factors, the modified first and second finite-length models for radial motion can be summarized as

$$F_n = -12L_s^n\left(\frac{R}{L}\right)^2\left(\alpha_{v1}^n C_1 C_v^n \dot{e} + C_2 M_{un}^n \ddot{e} + C_2 M_{cv}\frac{\dot{e}^2}{e}\right) \tag{28}$$

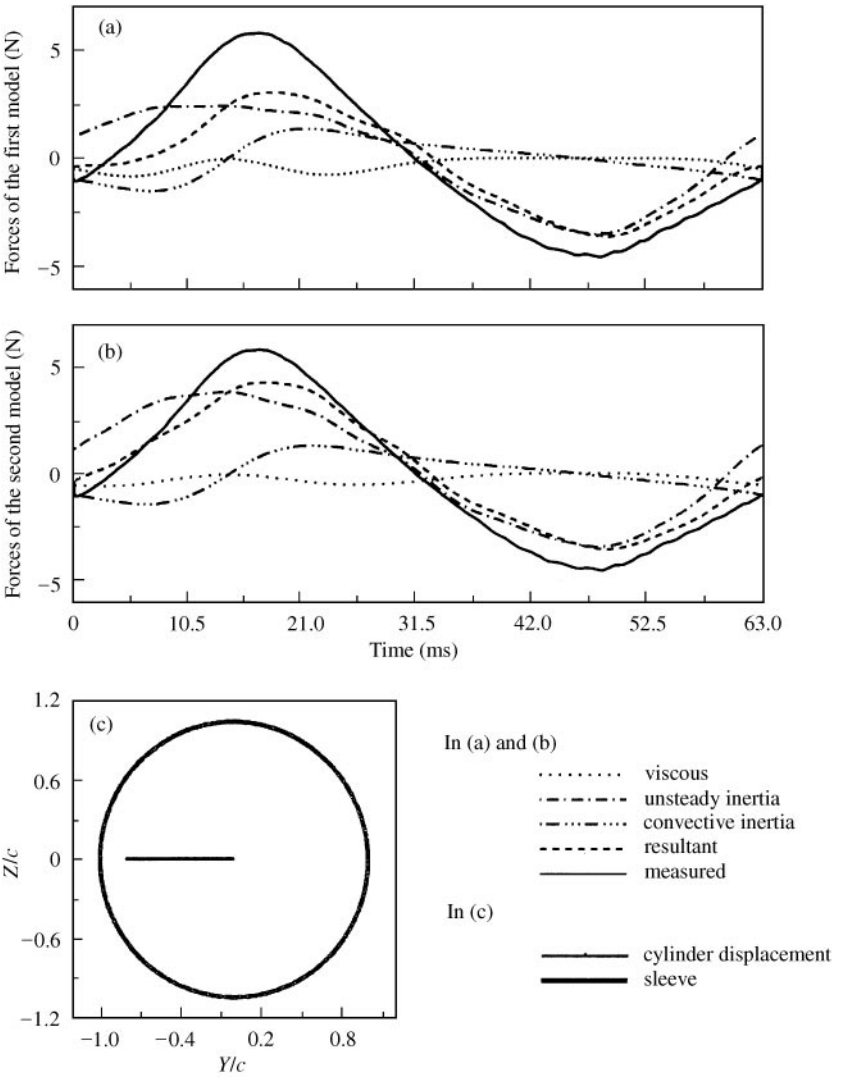

Figure 6. Displacements of LG cylinder centre and squeeze-film forces of the two finite-length models for radial motion for $f = 16$ Hz, $\varepsilon_i = 0{\cdot}4$ and $\varepsilon_o = 0{\cdot}4$.

and

$$F_n = -C_1 C_v^n L_v^n \dot{e} - \alpha_{u2}^n C_2 M_{un}^n L_{un}^n \ddot{e} - C_2 M_{cv} L_{cv} \frac{\dot{e}^2}{e}, \tag{29}$$

where in equation (28)

$$L_s^n = \frac{1}{(b_n/\alpha_{L1})^2}\left(1 - \frac{\tanh(b_n L/D\alpha_{L1})}{b_n L/D\alpha_{L1}}\right) \tag{30}$$

and $\alpha_{v1}^n (= f/36 + 0{\cdot}2)$ and α_{L1} $(= 2)$ are correction factors for the viscous term and length-correction factor in the normal force for the first model. The effect of α_{L1} is to increase L_s^n somewhat so that $12(R/L)^2\ L_s^n$ is closer to unity; α_{u2}^n $(= 1{\cdot}3)$ is the correction factor for the unsteady inertia term in the normal force for the second model.

Figure 7 gives the multiple determination coefficients R^2 for the modified theoretical predictions for all 20 experimental cases of radial motions with initial eccentricities. It is clear that the theoretical predictions by the present models are improved after modification. The predictions fit the measurements very well for $f = 8$, 16 and 32 Hz except one case with $\varepsilon_i = 0{\cdot}6$, $\varepsilon_o = 0{\cdot}3$ and $f = 32$ Hz, for which clear under-predictions around the peaks for all three models remain. Also, for the cases with low frequency $f = 4$ Hz, the R^2 values are still not very good. By studying equation (25) and Figure 4(a), we see that part of the reason for the lower R^2 values is due to the low values of the measured forces at 4 Hz.

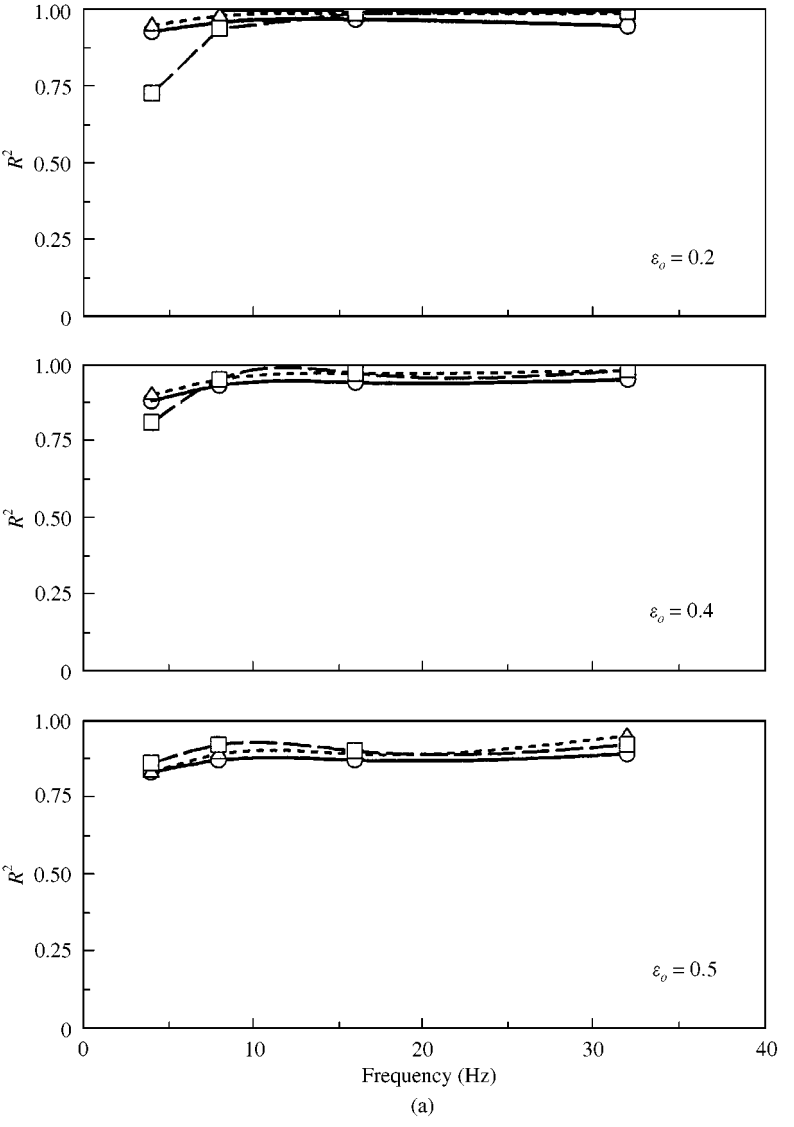

Figure 7. R^2 for LG radial motions with modified models (a) $\varepsilon_i = 0{\cdot}4$; (b) $\varepsilon_i = 0{\cdot}6$; —○—, Lu's model; - - -△- - -, modified 1st finite; —□—, modified 2nd finite.

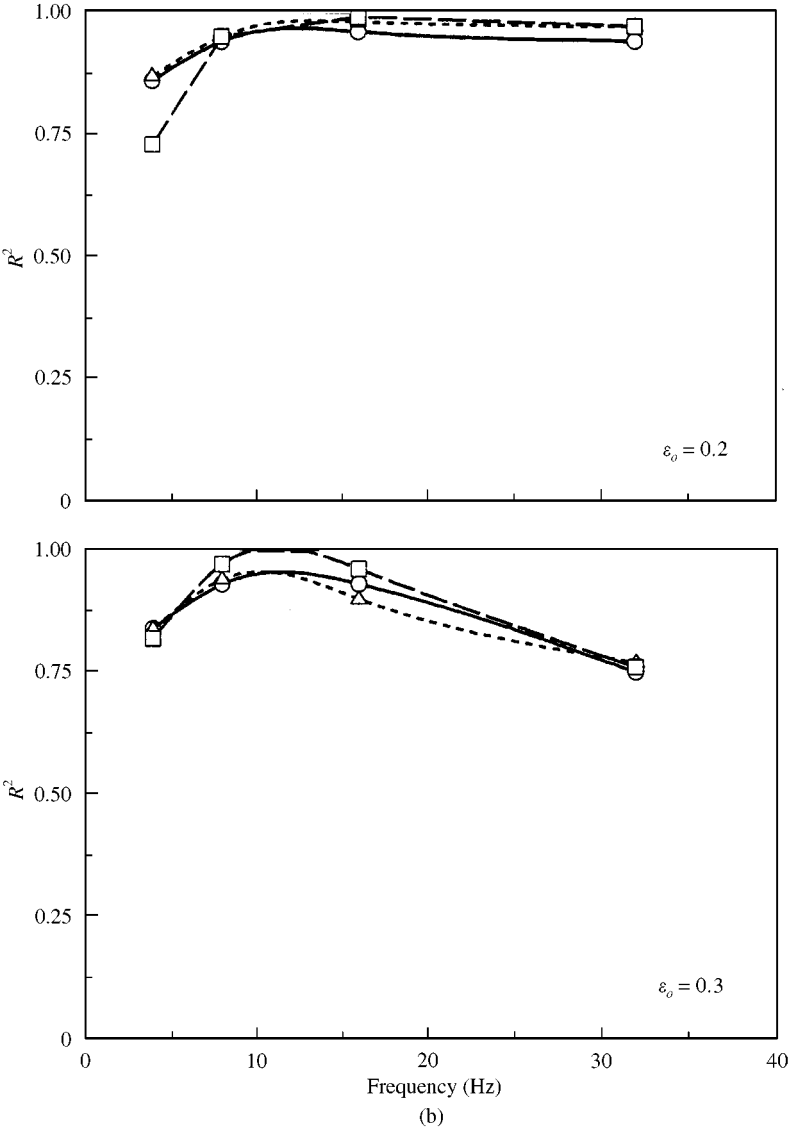

Figure 7. Continued

5.2. Radial Motions with Small Geometry

To further validate the theoretical predictions for radial motions, more experimental tests were conducted with the small geometrical configuration. There were 12 experimental cases with zero initial eccentricity and 12 with initial eccentricity as shown in Table 3. Figure 8 shows the experimental and predicted force waveforms for radial motions with zero initial eccentricity and nondimensional oscillation amplitude $\varepsilon_o = 0{\cdot}6$. Figure 9 presents the multiple determination coefficients for the 12 cases with initial eccentricity.

The reasonably good agreement between the theoretical predictions and the measured results (except for some cases with $f = 8$ and 64 Hz) demonstrates that the present models (especially the second model) are also quite reasonable for radial motion for the small

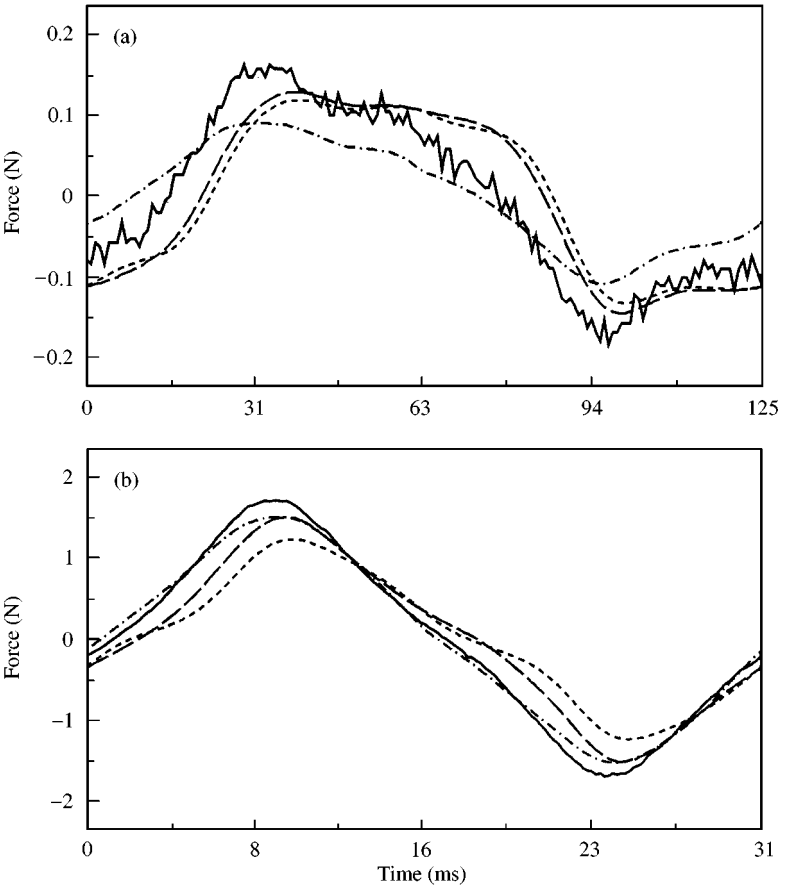

Figure 8. SG squeeze-film forces for radial motion with $\varepsilon_o = 0{\cdot}6$: (a) $f = 8$ Hz; (b) $f = 32$ Hz; ——, Measured; ·–·–·, Lu's model; - - - -, 1st finite; — —, 2nd finite.

geometry. The phase shift and the noise in the measured force waveforms observed for the large geometry for cases with low frequencies are still present. Because of the small force levels for the small geometry, the noise is substantial at low frequencies. One other point that should be mentioned here is the weakness of the multiple determination coefficient for the force waveforms of low magnitude and close to zero mean. Some R^2 values are rather low even though the waveforms are not so different for the cases with low frequencies.

Comparisons were also made using the modified force equations given by equations (28) and (29). Figure 10 shows the multiple determination coefficients R^2 of the modified theoretical predictions for the 12 experimental cases with initial eccentricity. From the graphs, one can see clearly that, except for case with $\varepsilon_i = 0{\cdot}6$, $\varepsilon_o = 0{\cdot}2$ and $f = 64$ Hz, both present theoretical predictions are improved after the modifications.

6. EXPERIMENTAL RESULTS AND COMPARISONS FOR OFFSET-LINEAR MOTIONS

In this section, experimental studies for the cylinders performing sinusoidal motions in the vertical direction, with initial eccentricities only in the horizontal direction (called offset-linear motions), are reported. There were 52 cases with the large geometry and another 52

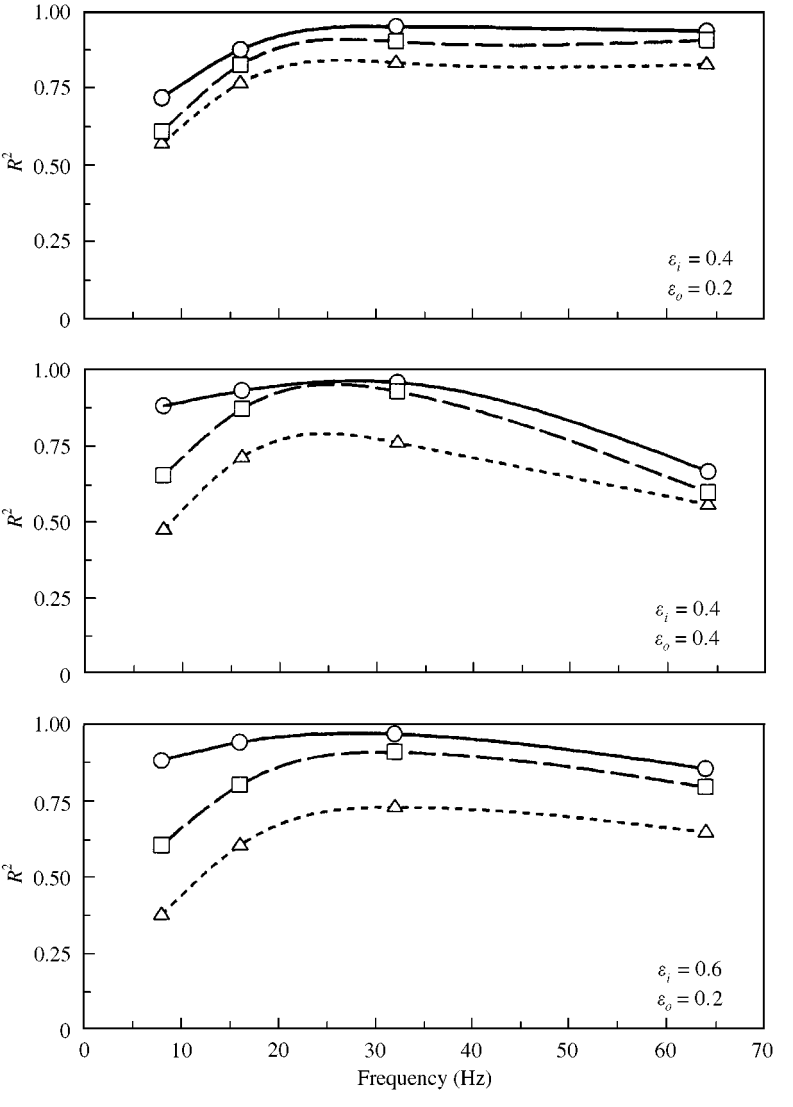

Figure 9. R^2 for SG radial motions; —○—, Lu's model; - - -△- - -, first finite; —□—, second finite.

cases with the small geometry as shown in Table 3. The measured force waveforms are converted to normal and tangential components for comparison with the predicted finite-length models given by equations (16) and (17) for the first model and equations (22) and (23) for the second model.

The force waveforms are also compared with the predictions from the Lu & Rogers' (1995) modified short model which was developed using the large-geometry apparatus and can be expressed as

$$F_n = -\alpha_{1n}\mathrm{Re}_{i_n} C_1 C_v^n \dot{e} - \alpha_{2n} C_2 M_{un}^n \ddot{e} - \alpha_{3n} C_2 M_{cv} \dot{e}^2/e - \alpha_{4n} C_2 M_{ce} e\dot{\psi}^2,$$

$$F_t = -\alpha_{1t}\mathrm{Re}_{i_t} C_1 C_v^t e\dot{\psi} - \alpha_{2t} C_2 M_{un}^t e\ddot{\psi} - \alpha_{3t} C_2 M_{co}\, 2\dot{e}\dot{\psi}, \tag{31}$$

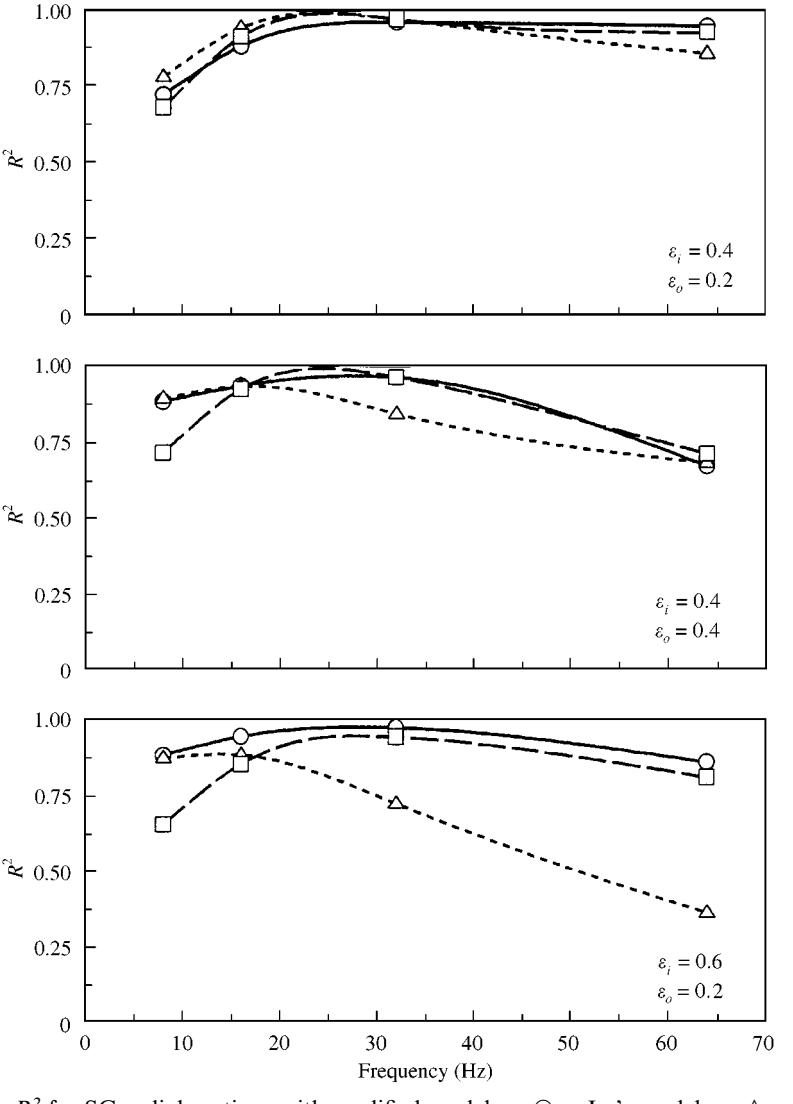

Figure 10. R^2 for SG radial motions with modified models; —○—, Lu's model; - - -△- - -, modified 1st finite; —□—, modified 2nd finite.

TABLE 4
The average correction factors for Lu's modified short model

Normal force		Tangential force	
α_{1n}	0·02	α_{1t}	0·01
α_{2n}	0·88	α_{2t}	1·04
α_{3n}	0·60	α_{3t}	1·05
α_{4n}	0·87		

where

$$\mathrm{Re}_{i_n} = \frac{\rho |v_n| c}{\mu} \quad \text{and} \quad \mathrm{Re}_{i_t} = \frac{\rho |v_t| c}{\mu}$$

are instantaneous squeeze-film Reynolds numbers for the normal and tangential direction forces. $|v_n|$ and $|v_t|$ are the absolute values of the normal and tangential velocities. C_1 and C_2 are geometry coefficients and C_v^n, M_{un}^n, M_{cv}, M_{ce}, C_v^t, M_{un}^t and M_{co} are nonlinear force coefficients given by Lu & Rogers (1995). The α_{in} and α_{it} are the average correction factors for all experimental cases with offset-linear motion and are listed in Table 4.

6.1. Offset-Linear Motions with Large Geometry

Figure 11 presents typical forces for the case with initial eccentricity $\varepsilon_i = 0{\cdot}4$ and amplitude $\varepsilon_o = 0{\cdot}6$. The theoretical predictions are quite good for Lu's model and the present second model, especially the tangential forces, whereas the first model produces lower force

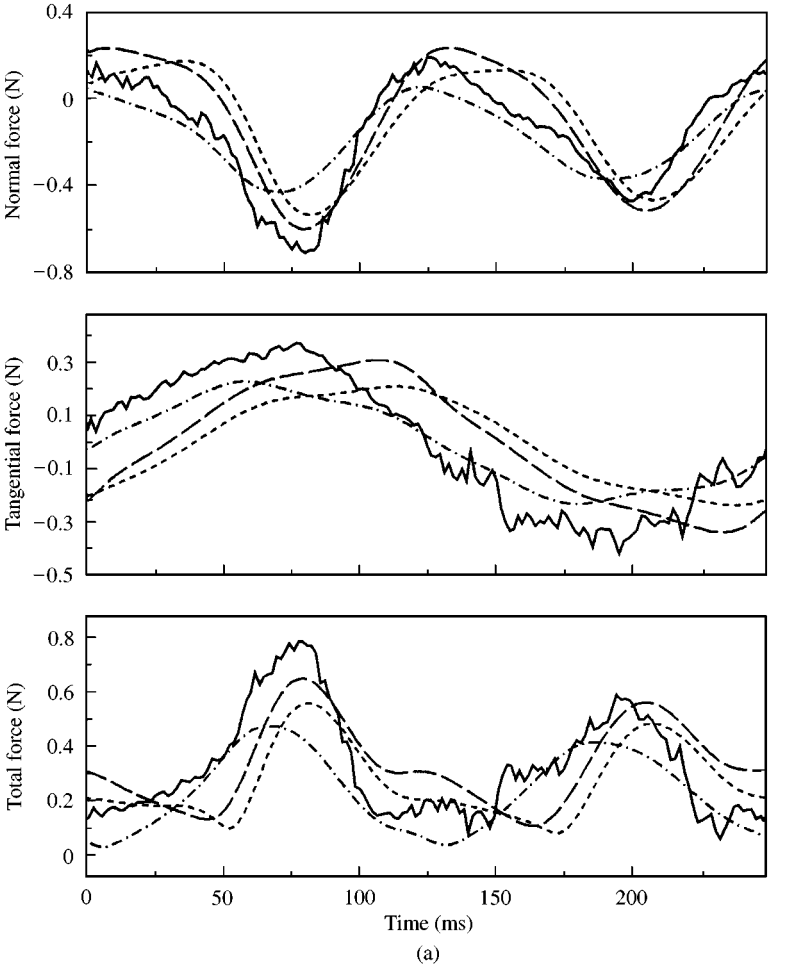

Figure 11(a). LG force waveforms for offset-linear motion with $f = 4$ Hz, $\varepsilon_i = 0{\cdot}4$ and $\varepsilon_o = 0{\cdot}6$; ——, Measured; ·–·–·, Lu's modified short; ------, 1st finite; — — —, 2nd finite.

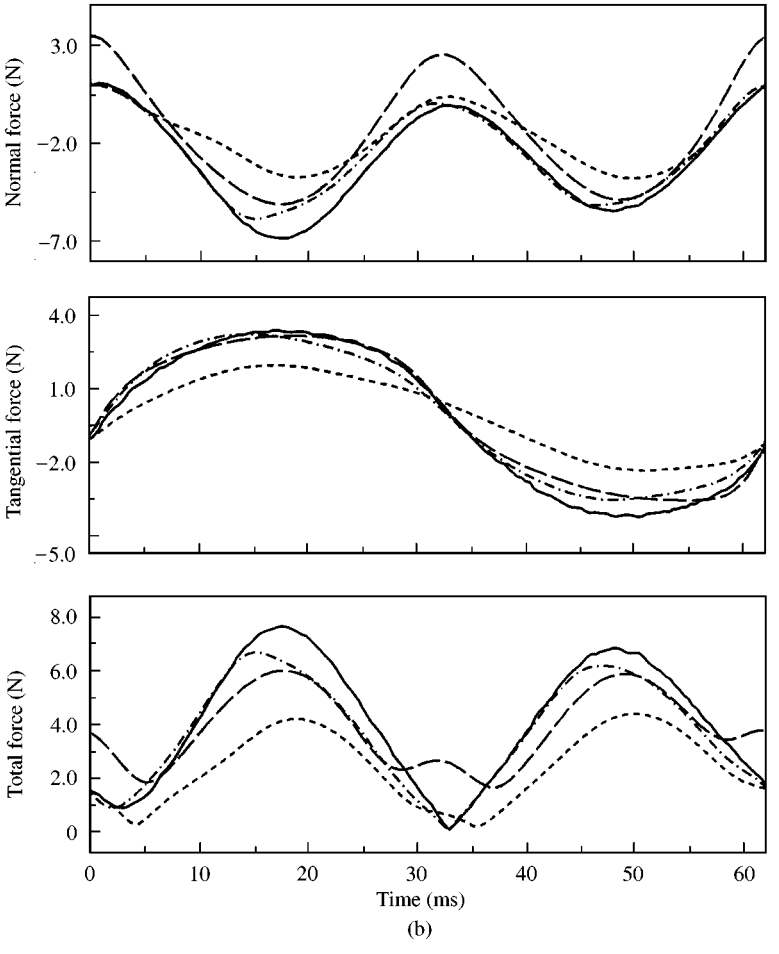

Figure 11(b). LG force waveforms for offset-linear motion with $f = 16$ Hz, $\varepsilon_i = 0{\cdot}4$ and $\varepsilon_o = 0{\cdot}6$; ——, Measured; ·–·–·–·, Lu's modified short; ------, 1st finite; — — —, 2nd finite.

predictions. All three models become less accurate as the total vibration amplitude or the frequency increases. For lower frequencies, when the total instantaneous eccentricity increases, the under-prediction from Lu's model becomes greater, while the phase shift of the present models becomes smaller. As the frequency increases, the differences among the three theoretical predictions increase for the cases with larger total amplitudes. The deviations of the predicted total force around the waveform valleys for the second model become larger as the total vibration amplitude or vibration frequency increases.

The multiple determination coefficients for Lu's modified short model and the two present finite-length models for 12 cases with $\varepsilon_i = 0{\cdot}4$ are shown in Figure 12. To show the overall level of agreement, Table 5 lists the mean and standard deviation values of the determination coefficients for each model for all 52 large geometry cases. Lu's modified short model has a mean coefficient of 0·950, the second model is relatively close at 0·913, while the first model is lowest at 0·798. As the amplitude or the initial eccentricity increases, the errors tend to be somewhat larger, especially for the first model.

In the previous section for radial motion, the normal force equations of the two present models are each modified slightly by using constant or linearly varying correction factors. Similar modifications are now presented for the offset-linear motion tests, in order to

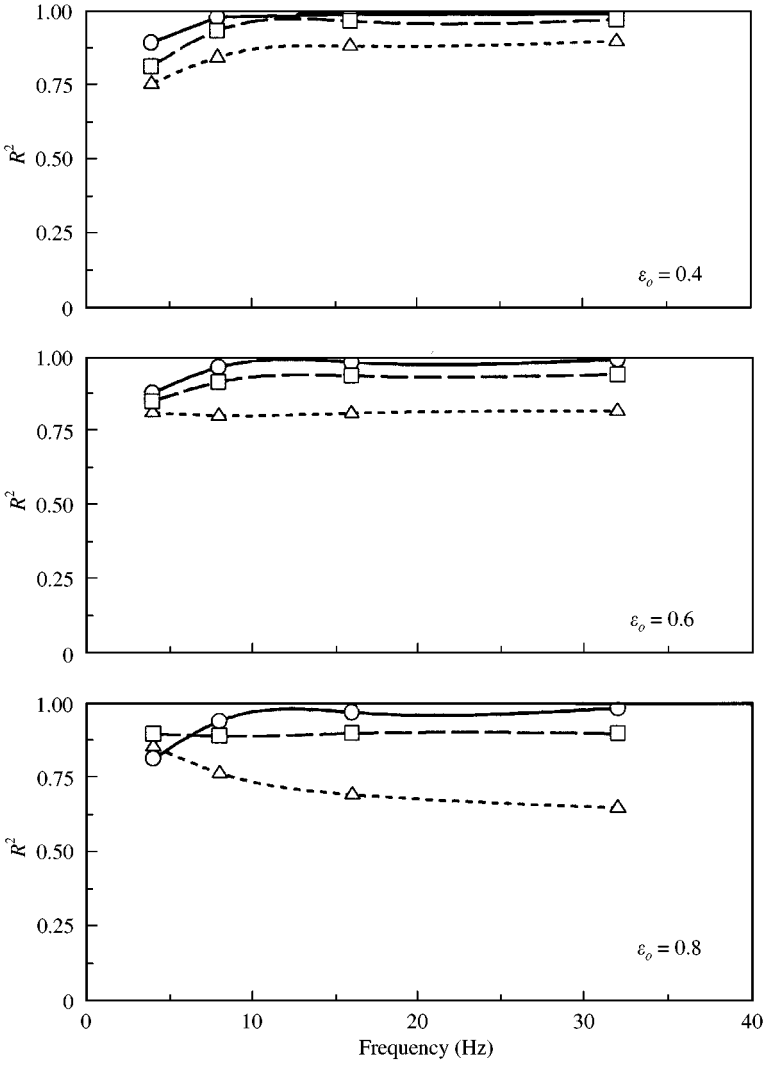

Figure 12. R^2 for LG offset-linear motions with initial eccentricity $\varepsilon_i = 0{\cdot}4$; —○—, Lu's model; - - -△- - -, 1st finite; —□—, 2nd finite.

TABLE 5
Average determination coefficients for total force waveforms for offset-linear motions

	Large Geometry (52 cases)		Small Geometry (52 cases)	
Model	Mean R^2	Standard dev.	Mean R^2	Standard dev.
Lu's modified short	0·950	0·055	0·845	0·139
First finite	0·798	0·063	0·706	0·236
Second finite	0·913	0·049	0·829	0·168
Modified first finite	0·936	0·042	0·797	0·305
Modified second finite	0·968	0·031	0·923	0·094

improve the prediction accuracy and also to explore the weaknesses of the models. From the results in this section, one can see that the following need improvement:

(i) the under-prediction of the normal forces for both models and the tangential forces for the first model, for motions with large amplitude and high frequency;
(ii) the deviations around the waveform peaks in the normal forces for cases with large amplitude and high frequency for the second finite-length model;
(iii) the phase shifts in the tangential forces for both models and in the normal forces for the first model at low frequency.

The task of modifying the two general theoretical equations looks much more complicated than for the equations for radial motion. A clear understanding of the contributions of each force component term for various frequencies and vibration amplitudes becomes prerequisite to understanding the squeeze-film forces and building better models. As an example, Figure 13 presents the individual force term waveforms, their resultant forces and the measured forces in the normal and tangential directions for the second finite-length model for $f = 8$ Hz, $\varepsilon_i = 0{\cdot}4$ and $\varepsilon_o = 0{\cdot}6$. The displacement of the cylinder centre is also displayed. In this example, the trace of the cylinder centre forms a narrow figure eight. At higher frequencies, the path has a narrow ellipse-like form. The small oscillations of the cylinder centre in the Y direction are due to various complicated inertia effects, slight misalignment and other unseen problems. This effect is fully taken into account in the force calculations since the equations use the actual cylinder motions in both directions.

By comparing the force terms, their resultant and measured forces in the normal and tangential directions, we found the following.

(i) Since the unsteady inertia term is always dominant over the other terms, the underprediction of the total force is mainly due to the unsteady inertia force term in the normal direction. Therefore, the deviations can be reduced by increasing the normal-direction unsteady inertia term.
(ii) Around the valleys of the total force waveforms, the normal viscous and convective inertia terms pass through zero, while the normal unsteady and centripetal inertia terms become the only contributors to the resultant forces, but with opposite signs. This suggests that the magnitude of centripetal inertia term needs to be increased.
(iii) The phase shift of the normal and tangential forces is mainly affected by the viscous terms. At low frequency, the contributions of the viscous and unsteady inertia terms are comparable and the phase shift of the predicted force waveforms with respect to the measured waveforms is positive. As the frequency increases, the relative contribution of the viscous term decreases and the unsteady inertia term becomes the dominant term, so that the phase shift decreases and becomes negative for $f = 32$ Hz. In other words, the viscous term is over-predicted for low-frequency motion and under-predicted at high frequency. This behaviour of the viscous force is very similar to what Lu & Rogers (1995) found. El-Shafei (1988) also made similar statements.

To achieve the highest determination coefficients and avoid the deviations around the waveform valleys in the total forces, three correction factors are used for each finite-length model. The modified first finite-length model is expressed as

$$F_n = -12\left(\frac{R}{L}\right)^2\left(\alpha_{v1}^n L_s^n C_1 C_v^n \dot{e} + L_s^n C_2 M_{un}^n \ddot{e} + L_s^n C_2 M_{cv}\frac{\dot{e}^2}{e} - L_s^t C_2 M_{ce} e\dot{\psi}^2\right), \quad (32)$$

$$F_t = -12\left(\frac{R}{L}\right)^2\left(\alpha_{v1}^t L_s^t C_1 C_v^t e\dot{\psi} + L_s^t C_2 M_{un}^t e\ddot{\psi} + (L_s^n + L_s^t) C_2 M_{co}\dot{e}\dot{\psi}\right), \quad (33)$$

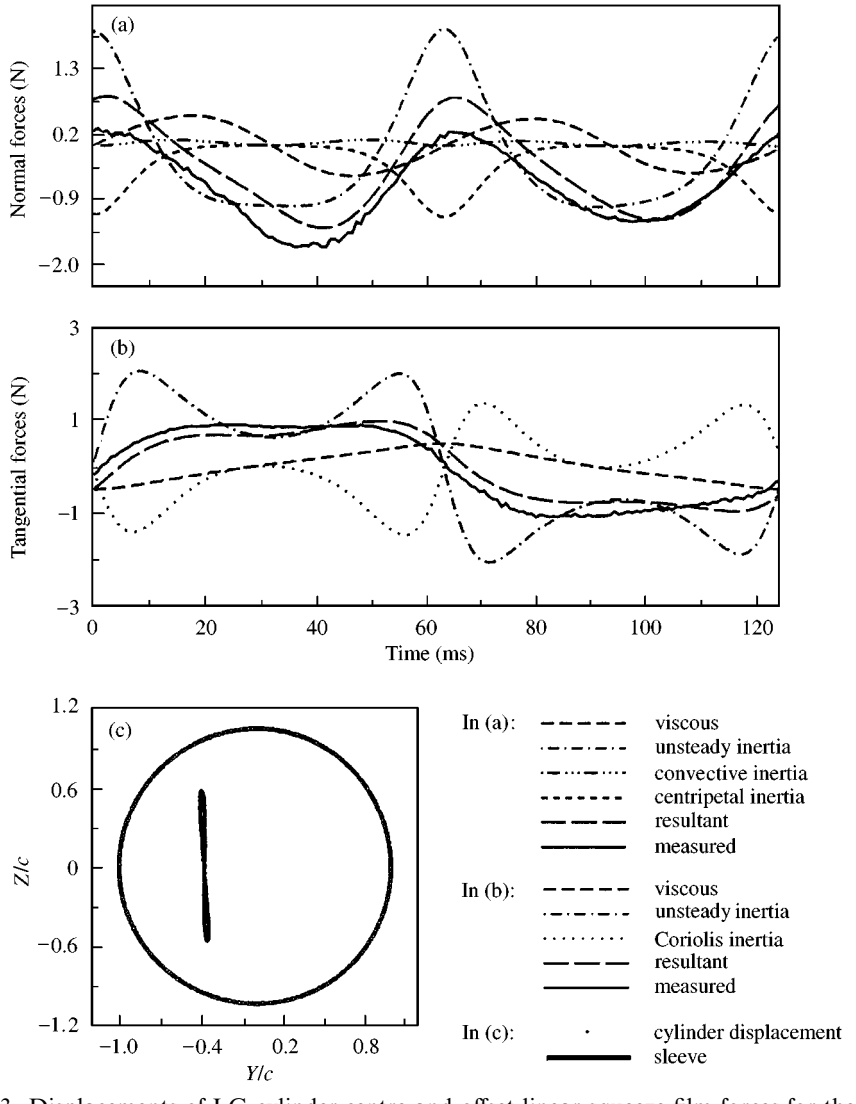

Figure 13. Displacements of LG cylinder centre and offset-linear squeeze film forces for the second finite length model for $f = 8$ Hz, $\varepsilon_i = 0{\cdot}4$ and $\varepsilon_o = 0{\cdot}6$.

TABLE 6
Correction factors for the modified first and second finite length model

First finite-length model		Second finite-length model	
α_{v1}^n	$f/36 + 0{\cdot}2$	α_{v2}^t	$f/36 + 0{\cdot}2$
α_{v1}^t	$f/36 + 0{\cdot}2$	α_{u2}^n	1·3
α_{L1}	2	α_{ce2}	1·3

where L_s^m ($m = n$ or t) is given by equation (30) where b_n becomes b_m, and α_{v1}^n and α_{v1}^t are correction factors for the viscous terms in the normal and tangential forces. The modified expressions for the second finite-length model are

$$F_n = -C_1 C_v^n L_v^n \dot{e} - \alpha_{u2}^n C_2 M_{un}^n L_{un}^n \ddot{e} - C_2 M_{cv} L_{cv} \frac{\dot{e}^2}{e} + C_2 (M_{ce} + \alpha_{ce2}) L_{ce} e\dot{\psi}^2, \quad (34)$$

$$F_t = -\alpha_{v2}^t C_1 C_v^t L_v^t e\dot{\psi} - C_2 M_{un}^t L_{un}^t e\ddot{\psi} - C_2 M_{co} L_{co}\, 2\dot{e}\dot{\psi}, \quad (35)$$

where α_{v2}^t, α_{u2}^n and α_{ce2} are correction factors for the viscous term in the tangential force and the unsteady and centripetal inertia terms in the normal force, respectively.

The best values or expressions for the correction factors were found by trial and error and are listed in Table 6. [Time constraints made impractical the use of more rigorous least-squares procedures, such as that used by Lu & Rogers (1995)]. The same values as used for radial motions are again used here. Unlike the other factors, α_{ce2} is a constant factor added to the inertia force coefficient M_{ce}. The value of α_{ce2} was obtained through comparison of the force coefficients M_{ce} from the present second model and the study by San Andres & Vance (1986), as well as by trial and error.

Figure 14 shows examples of measured and predicted force waveforms using the two modified finite-length models for $\varepsilon_i = 0{\cdot}4$, $\varepsilon_o = 0{\cdot}6$ and $f = 4$ and 16 Hz. Compared to the waveforms in Figure 11, the agreement has clearly improved. Since it is not easy to know the frequency when simulating the motion of a heat exchanger tube, the same cases have also been run without the corrections to the viscous terms which are linear functions of frequency. Figure 15 shows that the agreement has worsened somewhat, especially for the first model at the lower frequency.

It was found that the values for all three correction factors for each model are very reasonable for almost all the cases conducted in the present study. We found that the unsteady inertia terms and the viscous terms in the normal direction behave in a very similar manner as in the radial motion cases. The greatest improvement to the theoretical prediction is made by increasing the unsteady inertia terms in both directions for the first model (using the length correction factor adjustment α_{L1}) and in the normal direction for the second model. The effects of the phase shift (in both models) and the deviation around the waveform valleys (in the second model only) on the total force are relatively small and can be neglected.

The multiple determination coefficients for cases of $\varepsilon_i = 0{\cdot}4$ with $\varepsilon_o = 0{\cdot}4$, 0·6 and 0·8 for the modified finite-length models are shown in Figure 16. Clearly, they are much improved compared to the values in Figure 12. The mean and standard deviation R^2 values for the two modified models for all 52 large-geometry cases are listed in Table 5. The values are substantially higher for the modified models and are quite reasonable.

6.2. Offset-Linear Motions with Small Geometry

This section presents the results for the 52 offset-linear experimental cases for the small geometrical configuration. Figure 17 shows typical force waveforms with initial eccentricity $\varepsilon_i = 0{\cdot}4$ and nondimensional oscillation amplitude $\varepsilon_o = 0{\cdot}6$. The predicted waveforms are based on the unmodified finite-length equations (16, 17) and (22, 23) and Lu's equations (31). Generally, the results of the measured and predicted forces are similar to those for the large geometrical configuration and are not bad.

The mean and standard deviation R^2 values are given in Table 5. The mean values for the small geometry are about 11% lower than those for the large geometry. For some cases with large oscillation amplitude, the agreement between the theoretical predictions and experimental measurements is poor. The worst R^2 values are from cases with $\varepsilon_i = 0{\cdot}7$ and $\varepsilon_o = 0{\cdot}5$.

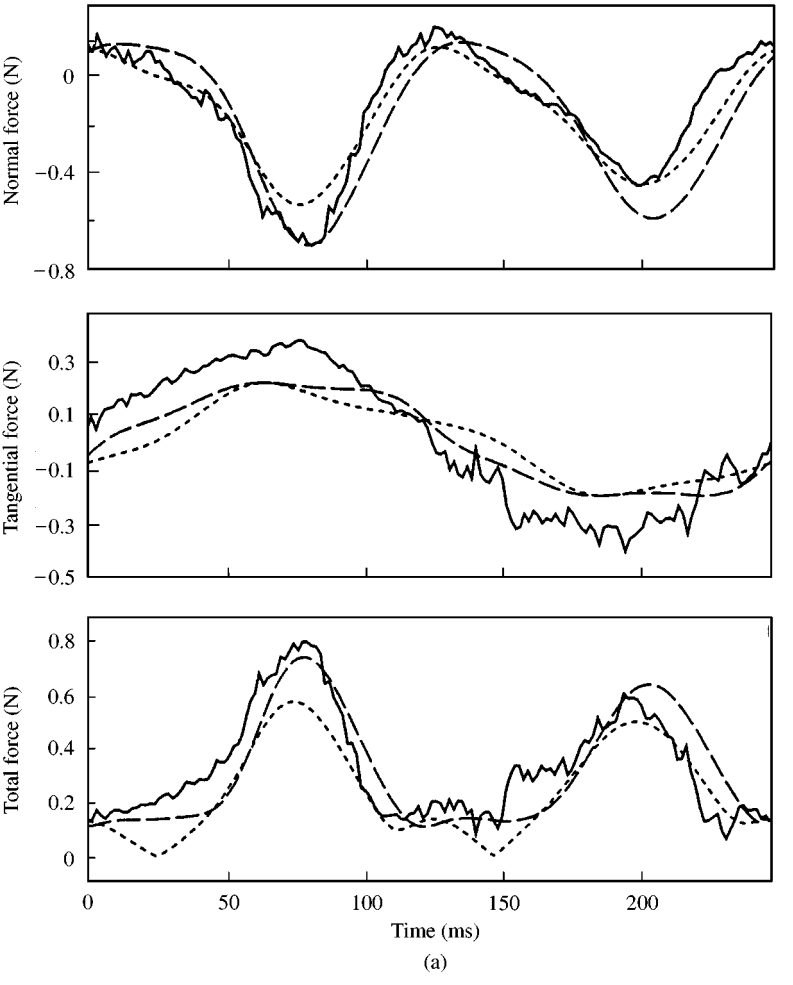

Figure 14. LG force waveforms for offset-linear motion with $\varepsilon_i = 0{\cdot}4$ and $\varepsilon_o = 0{\cdot}6$, where the present models are modified by all six correction factors: (a) $f = 4$ Hz; (b) $f = 16$ Hz; ——, Measured; ------, 1st finite; — — —, 2nd finite.

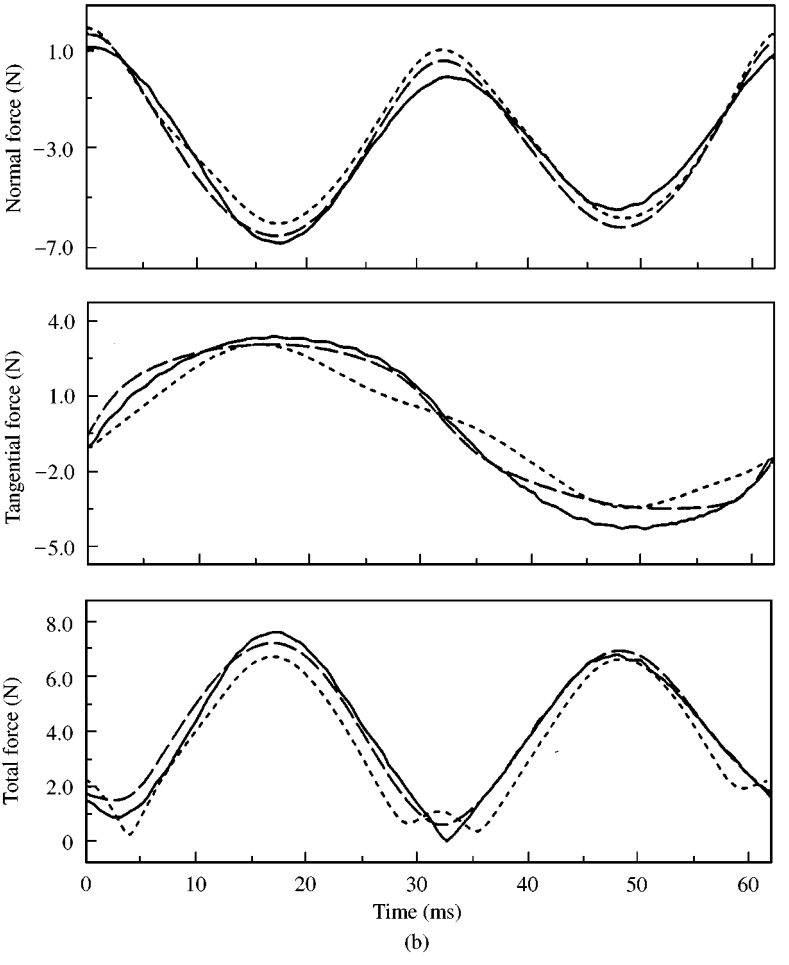

Figure 14. Continued

Part of the reason could be the alignment of the cylinder and its support sleeve. Due to the smaller size of the cylinder and the smaller clearance between the cylinder and the sleeve, the alignment for the small geometry is much more difficult than for the large one. Comparing predictions from the two present models with the measured forces, the second finite-length model clearly gives better values than the first model for all cases. The agreement between the measurements and the theoretical predictions from Lu's modified short model and the second finite-length model are at the same level; the second finite-length model has better predictions for $f = 8$ and 16 Hz, while Lu's modified short model gives slightly better predictions for $f = 32$ and 64 Hz.

The phase shifts reported in the preceding sections for the theoretical models are observed again for the offset-linear motions with the small geometry. At the lowest frequency, $f = 8$ Hz, the waveforms of the present models and Lu's model give the largest phase shifts with respect to the measured force waveforms of all the experimental cases conducted in the present study. The phase shifts in the total forces from the present models are positive and about 25–30°, whereas Lu's model gives negative phase shifts with values between 30 and 50°. As the frequency increases, the phase shift decreases. At $f = 64$ Hz, the

phase shifts are very small for the three models and can be neglected. This is attributable to the relative importance of the viscous terms at low frequencies and the fact that the ratio of the viscous terms to the unsteady inertia terms increases as the clearance (squared) decreases.

The calculated forces in the normal direction are not as good as those in the tangential direction. Compared with the normal direction forces for the large geometry, the normal direction forces for the small geometry have even clearer deviations around the waveform peaks between the theoretical and measured forces. Consequently, this causes deviations in the total theoretical forces from the measured total forces around the waveform valleys. As the frequency increases, the deviations become more obvious.

Based on the observations of the 52 cases and the comparisons of each force term (not presented in this paper), we found that equations (32)–(35) with the six correction factors

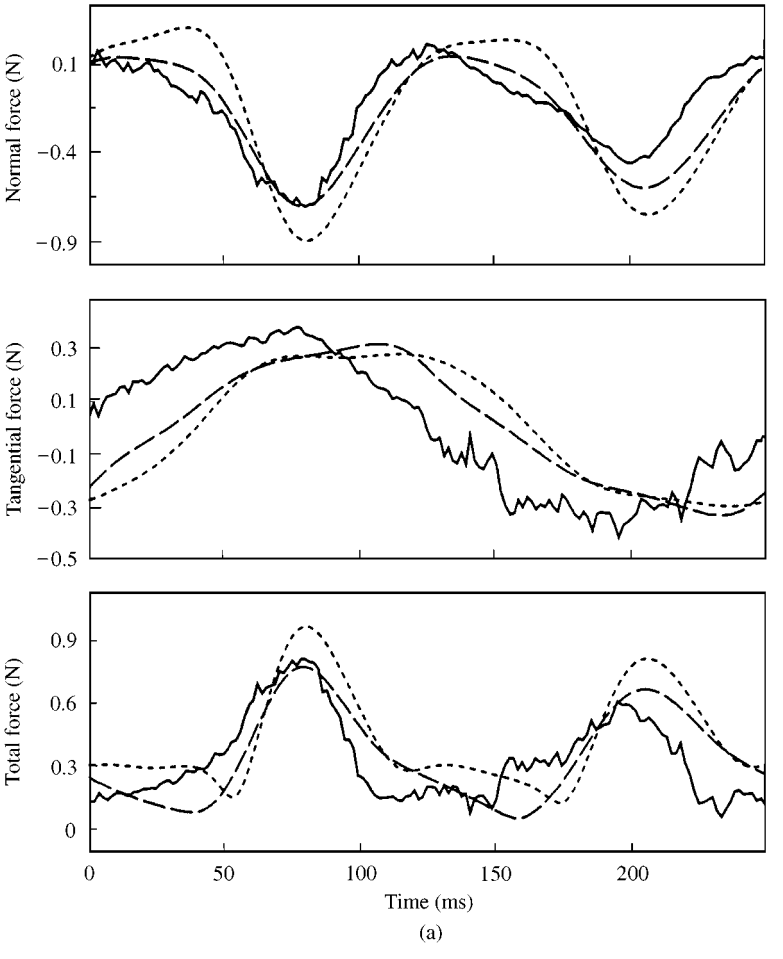

Figure 15. LG force waveforms for offset-linear motion with $\varepsilon_i = 0{\cdot}4$ and $\varepsilon_o = 0{\cdot}6$, where the present models are modified with three correction factors (without modifying the viscous terms): (a) $f = 4$ Hz; (b) $f = 16$ Hz; ——, Measured; - - - - - -, 1st finite; — — —, 2nd finite.

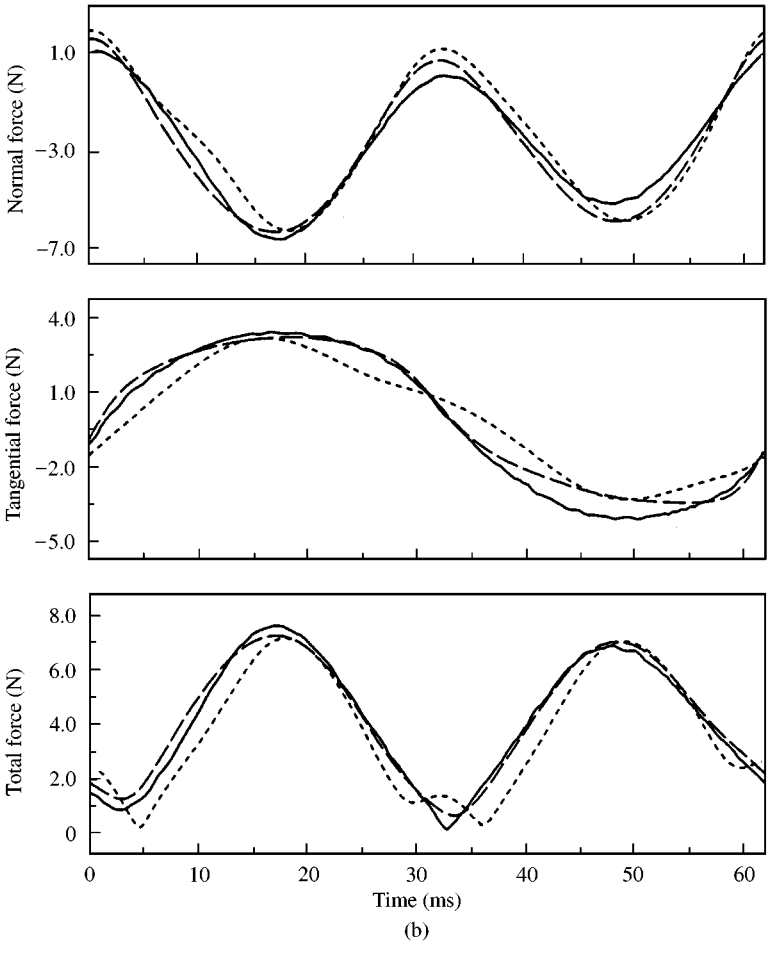

Figure 15. Continued

can still be used here to obtain improved theoretical predictions. The only difference in the factors shown in Table 6 is in the expressions for the three viscous factors where 36 is replaced by 64 (the maximum frequency). Using the six correction factors some improvement has been achieved, particularly for the total forces. The mean and standard deviation R^2 values for all 52 small-geometry cases for the modified equations are also listed in Table 5. The modified second finite-length model has a mean R^2 of 0·923 for the small geometry which is only 5% lower than for the large geometry. By comparison, the first model is not as good with the R^2 value 15% lower than that for the large-geometry value.

Overall, the agreement in the prediction of total force waveforms for the small geometry is fairly reasonable even though the normal force and tangential force tend to be substantially over-predicted and under-predicted, respectively.

7. CONCLUSIONS

Two nonlinear cylindrical squeeze-film force models have been derived for finite-length geometries for arbitrary cylinder motions. The first finite-length model is formed using

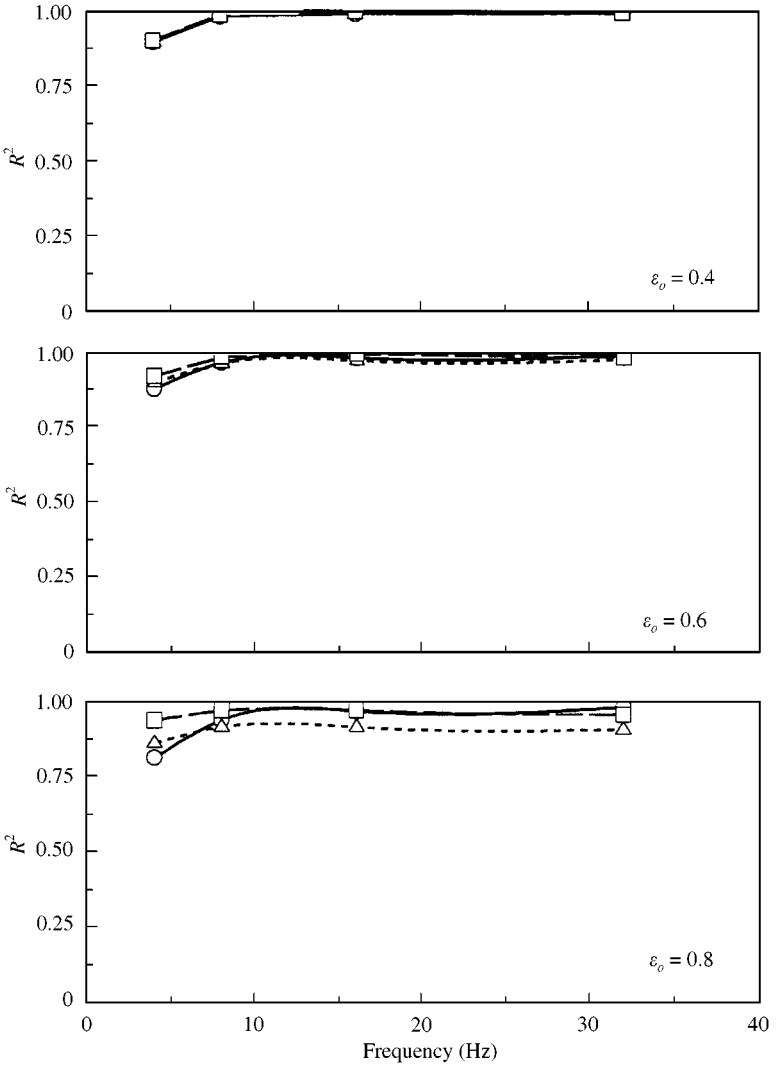

Figure 16. R^2 for LG offset-linear motions with modified models and $\varepsilon_i = 0{\cdot}4$; —○—, Lu's model; - - -△- - -, modified 1st finite; —□—, modified 2nd finite.

radial and tangential length-correction factors on a short model. The second finite-length model is constructed using side-leakage factors with an infinitely long model. In order to validate the models, 160 experimental case studies with two geometrical sizes have been undertaken. A multiple determination coefficient is used to statistically compare the force waveforms.

The experimental radial motion studies involved 24 cases with zero initial eccentricity and 32 cases with nonzero initial eccentricity. Typical experimental force waveforms and the theoretical predictions using the present finite length models and that of Lu & Rogers (1994) are presented. These tests involved only three of the seven nonlinear force terms in each model. Through investigations of each force term, the present finite-length models were modified slightly. The unmodified models are reasonably good in predicting squeeze-film forces for most of the cases conducted, while the modified models give improved prediction

accuracy and better results. Comparing the two present finite-length models, the second one, based on the long model, produces better agreement.

Similar results were obtained for 104 experimental cases where the initial eccentricity is perpendicular to the line of motion. The unmodified finite-length equations give quite good predictions for most cases. By exploring each force term, it was found that the correction factors from the radial tests are still reasonable. The final modified models each have three correction factors. In the first finite-length model, which is based on the short model, both the normal and tangential viscous terms have a factor which is a linear function of frequency, which decreases the viscous terms at low frequency. As well there is a factor which increases the effect of each length-correction factor. For the second finite-length model, which is based on the long model, the main correction is to the normal unsteady inertia term which is multiplied by 1·3. There is also an additive factor in the centripetal inertia term and a linear function of frequency in the tangential viscous term.

Han & Rogers (2001) showed (in Figure 5) that the two long-model tangential inertia force terms are very different from those reported by El-Shafei & Crandall (1991). The

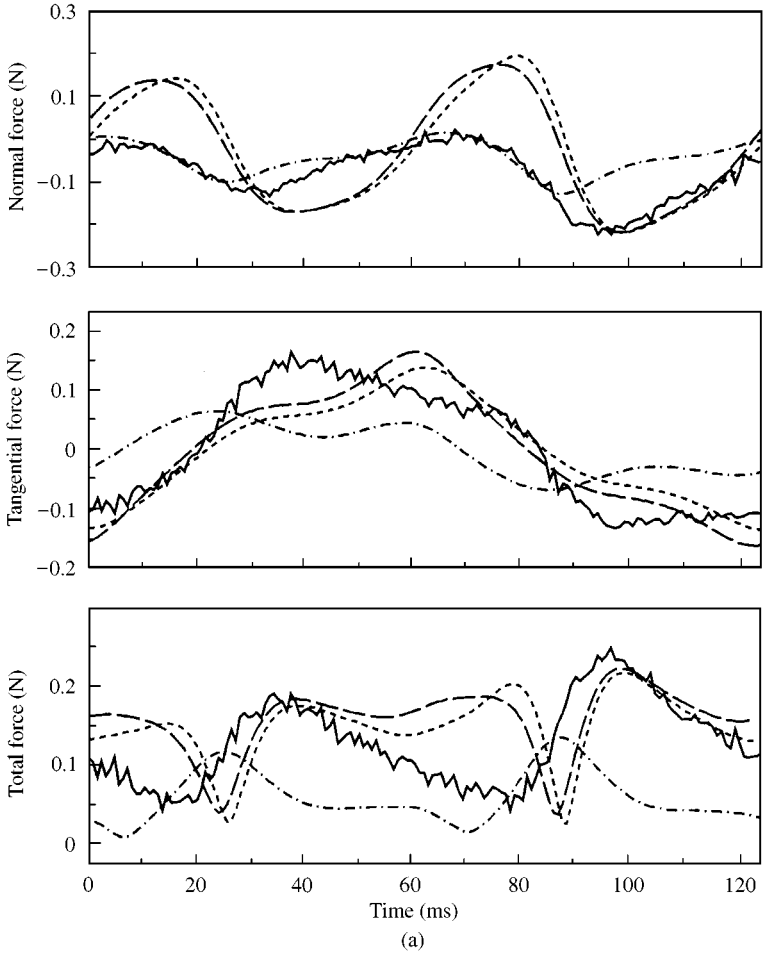

Figure 17(a). SG force waveforms for offset-linear motion with $f = 8$ Hz, $\varepsilon_i = 0{\cdot}4$ and $\varepsilon_o = 0{\cdot}6$; ——, Measured; ·–·–·–·, Lu's modified short; ------, 1st finite; — — —, 2nd finite.

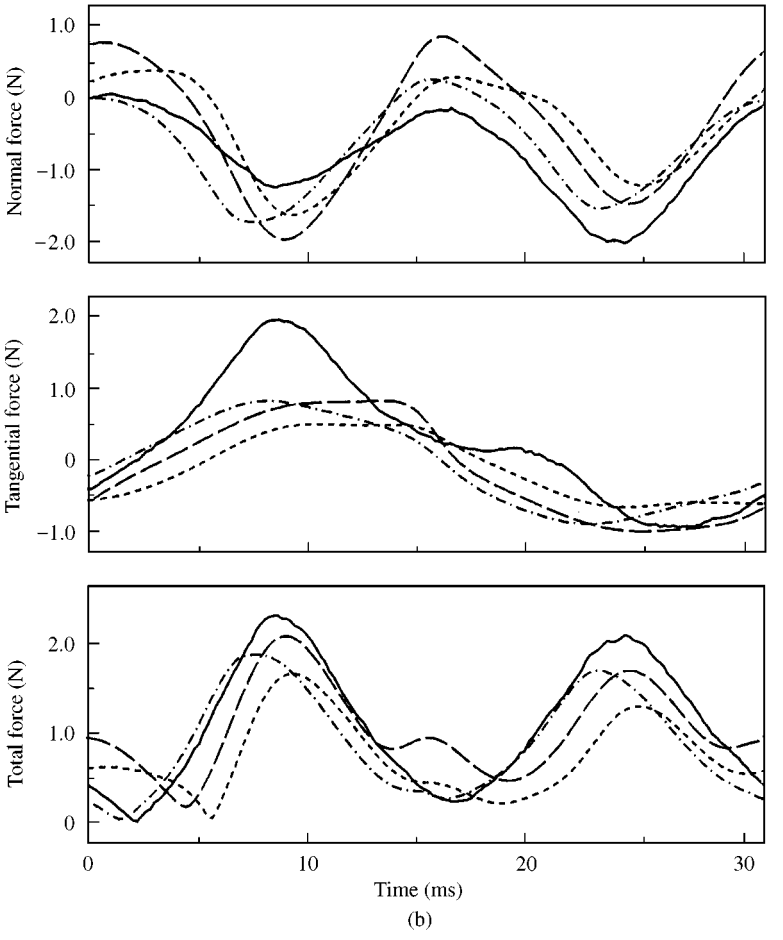

Figure 17(b). SG force waveforms for offset-linear motion with $f = 32$ Hz, $\varepsilon_i = 0{\cdot}4$ and $\varepsilon_o = 0{\cdot}6$; ——, Measured; ·–·–·–·, Lu's modified short; - - - - - -, 1st finite; — — —, 2nd finite.

present experimental results for the second model show indirectly that the Han and Rogers long model should be more accurate to predict squeeze-film forces, since no correction factors are needed to correct the tangential inertia force terms.

Lu and Rogers (1994, 1995) also observed a requirement to increase the normal unsteady inertia term by 30% and the need to have viscous terms which are linear functions of frequency. They hypothesized that these problems were due to the choice of a parabolic flow velocity profile, the approximation method used to derive the equations, and/or their edge effects modelling. The present work has shown that despite the use of analytical length-correction/side-leakage factors in order to obtain finite-length models, as well as the use of nonparabolic (elliptical) velocity profiles, and three different approximation methods (Han & Rogers 2001), similar weaknesses in the unsteady inertia terms and the viscous terms have been observed.

The observation that the viscous terms vary approximately linearly with frequency implies the presence of velocity-squared damping, e.g., a force term proportional to $\dot{e}|\dot{e}|$. This is commonly observed as the drag force on an object having motion relative to a fluid. Many experiments have shown that the flow separation around the body results in a pressure field which gives a drag force proportional to the velocity squared. This

behaviour has been observed previously in cylindrical squeeze films by Mulcahy & Miskevics (1980). Unfortunately the pressure field caused by flow separation cannot be predicted by models based on the Navier–Stokes equations. This effect can therefore only be included by empirical models obtained from experiments.

Similarly, theoretical modelling of the convective flows in and out of the squeeze film (i.e., edge effects) is also difficult or impossible to do. Although the present finite-length models are able to predict the squeeze-force waveforms quite well, it is now clear that the edge effects and velocity squared damping in cylindrical squeeze films typical of heat exchanger equipment cannot be accounted for by thorough modelling using Navier–Stokes equations, but instead require empirical testing.

ACKNOWLEDGEMENTS

The work reported here was supported by Atomic Energy of Canada Limited as part of its work on heat exchanger tube vibration and wear prediction. The authors also acknowledge the support of the Natural Sciences and Engineering Research Council of Canada and the University of New Brunswick.

REFERENCES

Arauz, G. L. & San Andres, L. A. 1993 Experimental pressures and film forces in a squeeze film damper. *ASME Journal of Tribology* **115,** 134–140.

Barrett, L. E., Allaire, P. E. & Gunter, E. J. 1980 A finite length bearing correction factor for short bearing theory. *ASME Journal of Lubrication Technology* **102,** 283–287.

Booker, J. F. 1965 A table of the journal-bearing integral. *ASME Journal of Basic Engineering* **87,** 533–535.

Burwell, J. T. 1951 The calculated performance of dynamically loaded sleeve bearings—III. *Journal of Applied Mechanics* **18,** 393–404.

Capone, G., D'Agostino, V. & Guida, D. 1994 A finite length plain journal bearing theory. *ASME Journal of Tribology* **116,** 648–653.

El-Shafei, A. 1988 Dynamics of rotors incorporating squeeze film dampers. Ph.D. dissertation, Department of Mechanical Engineering, Massachusetts Institute of Technology, Cambridge, MA, U.S.A.

El-Shafei, A. & Crandall, S. H. 1991 Fluid inertia forces in squeeze film dampers. In *Rotating Machinery and Vehicle Dynamics* **35,** 219–228. New York: ASME.

Falkenhagen, G. L., Gunter, E. J. & Schuller, F. T. 1972 Stability and transient motion of a vertical three-lobe bearing system. *ASME Journal of Engineering for Industry* **94,** 665–677.

Han, Y. 1997 Nonlinear fluid forces in cylindrical squeeze films. Ph.D. dissertation, Department of Mechanical Engineering, University of New Brunswick, Fredericton, Canada.

Han, Y. & Rogers, R. J. 1996 Squeeze film force modeling for large amplitude motion using an elliptical velocity profile. *ASME Journal of Tribology* **118,** 687–692.

Han, Y. & Rogers, R. J. 2001 Nonlinear fluid forces in cylindrical squeeze films. Part I: Short and long lengths. *Journal of Fluids and Structures* **15,** 151–170, doi: 10.1006/jfls. 2000.0324.

Haslinger, K. H., Martin, M. L. & Steininger, D. A. 1990 Experimental characterization of fluid and squeeze film effects in heat exchanger tube supports. *Journal of Fluids and Structures* **4,** 605–629.

Hays, D. F. 1959 A variational approach to lubrication problems and the solution of the finite journal bearings. *ASME Journal of Basic Engineering* **81,** 13–23.

Jung, S. Y., San Andres, L. A. & Vance, J. M. 1991 Measurements of pressure distributions and force coefficients in a squeeze film damper. Part I: fully open ended configuration. *Tribology Transactions* **34,** 375–382.

Kinsale, I. & Tichy, J. 1989 Numerical and experimental study of a finite submerged squeeze film damper. *Machinery Dynamics—Applications and Vibration Control Problems*, Vol. **18-2,** pp. 159–165. New York: ASME.

Lu, Y. 1993 Instantaneous squeeze film force between a heat exchanger tube and a support plate. Ph.D. dissertation, Department of Mechanical Engineering, University of New Brunswick, Fredericton, Canada.

Lu, Y. & Rogers, R. J. 1994 Normal instantaneous squeeze film force for a finite length cylinder. *ASME Journal of Tribology* **116,** 588–596.

Lu, Y. & Rogers, R. J. 1995 Instantaneous squeeze-film force between a heat exchanger tube and a support plate for arbitrary tube motion. *Journal of Fluids and Structures* **9,** 835–860.
Massey, B. S. 1977 A note on the theory of the short journal bearing. *International Journal of Mechanical Engineering Education* **5,** 95–96.
Mulcahy, T. M. 1980 Fluid forces on rods vibrating in finite length annular regions. *Journal of Applied Mechanics* **47,** 234–240.
Mulcahy, T. M. & Miskevics, A. J. 1980 Determination of velocity-squared fluid damping by resonant structural testing. *Journal of Sound and Vibration* **71,** 555–564.
Rogers, R. J., Berg, M. M., Rampen, W. H. S., Soh, Y. T., Teu, H. M. & Tin Kin Wang, T. K. V. 1990 Harmonic modelling of nonlinear fluid forces in finite length, cylindrical squeeze films. *Journal of Fluids and Structures* **4,** 583–603.
Rouch, K. E. 1990 Experimental evaluation of squeeze film damper coefficients with frequency domain techniques. *Tribology Transactions* **33,** 67–75.
San Andres, L. A. & Vance, J. M. 1986 Effects of fluid inertia and turbulence on the force coefficients for squeeze film dampers. *ASME Journal of Engineering for Gas Turbines and Power* **108,** 332–339.
San Andres, L. A. & Vance, J. M. 1987a Effects of fluid inertia on squeeze-film damper forces for small-amplitude circular-centered motions. *ASLE Transactions*, **30,** 63–68.
San Andres, L. A. & Vance, J. M. 1987b Force coefficients for open-ended squeeze-film dampers executing small-amplitude motions about an off-center equilibrium position. *ASLE Transactions* **30,** 69–76.
San Andres, L. A. & Vance, J. M. 1987c Experimental measurement of the dynamic pressure distribution in a squeeze-film bearing damper executing circular-centered orbit. *ASLE Transactions* **30,** 373–383.
Szeri, A. Z. 1980 *Tribology*, *Friction*, *Lubrication and Wear*. Washington, DC: Hemisphere Publishing, p. 59.
Tichy, J. A. 1984 Measurements of squeeze film bearing forces and pressures, including the effect of fluid inertia. *ASLE Transactions* **28,** 520–526.
Tichy, J. A. 1987 A study of the effect of fluid inertia and end leakage in the finite squeeze film damper. *ASME Journal of Tribology* **109,** 54–59..
Tolle, G. C. & Muster, D. 1969 An analytical solution for whirl in a finite journal bearing with a continuous lubricating film. *ASME Journal of Engineering for Industry* **91,** 1189–1195.
Tonnesen, J. 1976 Experimental parametric study of a squeeze film bearing. *ASME Journal of Lubrication Technology* **98,** 206–213.
Warner, P. C. 1963 Static and dynamic properties of partial journal bearings. *ASME Journal of Basic Engineering* **85,** 247–257.
Yu, S. & Rogers, R. J. 1991 Estimation of linearized force coefficients for cylindrical squeeze films. *Tribology Transactions* **34,** 308–317.
Zhang, J., Roberts, J. B. & Ellis, J. 1994 Experimental behavior of a short cylindrical squeeze film damper executing circular centered orbits. *ASME Journal of Tribology* **116**, 528–534.
Zhang, J. & Roberts, J. B. 1996 Solutions for the combined motion of finite length squeeze film dampers around the bearing center. *ASME Journal of Tribology* **118,** 617–622.

APPENDIX A: ERRATUM ON b_t^2

After the present work was completed, it was found that the expression used for b_t^2 from Barrett *et al.* (1980) is incorrect. The correct expression for b_t^2 is shown in equation (10). The incorrect expression for b_t^2 used in the present work is

$$b_t^2 = \frac{2+\varepsilon^2}{2\varepsilon^2}\left(2 + \frac{2+\varepsilon^2}{(1-\varepsilon^2)^{1/2}} - \frac{8+\varepsilon^2}{(4-\varepsilon^2)^{1/2}}\right). \tag{A1}$$

Comparisons of values of the tangential length-correction factor L_s^t (for the first finite length model) for a wide range of eccentricities for $L/D = 1$ have been carried out. The new L_s^t values are only slightly larger than the old values for low eccentricities. For example, the

new L_s^t value is less than 5% larger for eccentricities up to 0·67 and only 15% larger for $\varepsilon = 0{\cdot}8$.

The effect of the error in b_t^2 is therefore considered small.

APPENDIX B: NOMENCLATURE

A	shape factor of elliptical velocity profile (ratio of ellipse minor axis to h)
c	radial clearance
C_i	geometry coefficients, $i = 1, 2$
C_v	viscous (damping) force coefficient
D, R	cylinder diameter and radius
D_i	constant force coefficients, $i = 1, 2, 3, 4$
e	instantaneous displacement of cylinder centre
$\dot{e}$, $\ddot{e}$	instantaneous velocity and acceleration of the cylinder centre
f	oscillation frequency
F	squeeze-film force on the cylinder
h	instantaneous local squeeze-film thickness
L	cylinder length
LG, SG	large (50·6 mm) and small (25 mm) geometrical configurations
L_l^m	side-leakage factor for long model; $l = v$, *un*, *cv*, *ce*, *co*; $m = n$ or t
L_s^m	length-correction factor for short model; $m = n$ or t
M_{ce}	centripetal inertia force coefficient
M_{co}	Coriolis inertia force coefficient
M_{cv}	convective inertia force coefficient
M_{un}	unsteady inertia force coefficient
p	pressure in squeeze film
p_a	pressure far from the film edge
p_c	mid-plane pressure
Re	squeeze-film Reynolds number ($\mathrm{Re} = \omega c^2/v$)
R^2	multiple determination coefficient (equation (25))
X, Y, Z	fixed coordinate directions (Figure 1)
α_i^m	correction factors; $i = L1$, $v1$, $ce2$, $u2$, $v2$; $m = n$, t or nothing
γ	$(1 - \varepsilon^2)^{1/2}$
ε	instantaneous eccentricity ratio e_i/c
ε_i	initial eccentricity ratio e_i/c
ε_o	nondimensional oscillation amplitude (reference length c)
θ, φ	angles (Figure 1)
λ_l	eigenvalues of leakage factors; $l = v$, *un*, *cv*, *ce*, *co*
μ	absolute fluid viscosity
v	kinematic fluid viscosity
ρ	fluid mass density
ψ, $\dot{\psi}$, $\ddot{\psi}$	instantaneous angle, angular velocity and acceleration of cylinder centre
ω	characteristic circular frequency